

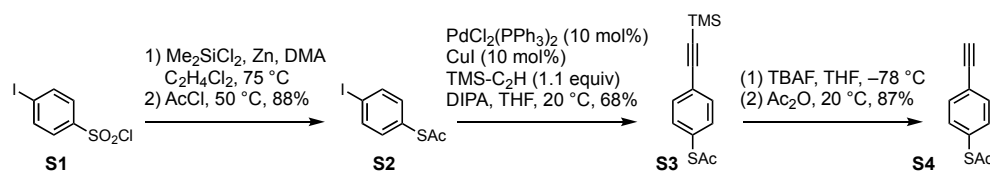
Cross-conjugation increases the conductance of *meta*-connected fluorenones

Asma Alanazy[†], Edmund Leary^{†*}, Takayuki Kobatake[†], Sara Sangtarash^{†*}, M. Teresa González, Hua-Wei Jiang, Gabino Rubio-Bollinger, Nicolás Agrait, Hatef Sadeghi, Iain Grace, Simon J. Higgins^{*}, Harry L. Anderson^{*}, Richard J. Nichols^{*}, and Colin J. Lambert^{*}

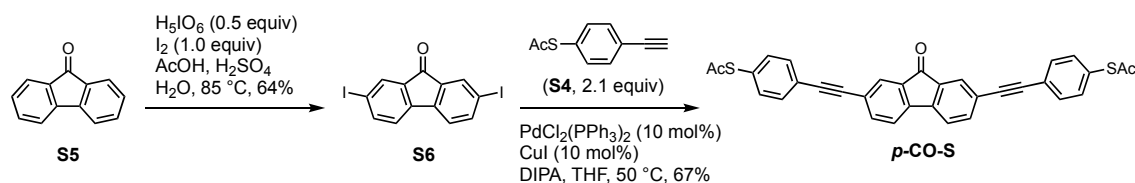
Table of Contents

Section 1	Synthetic Schemes	page S2–S3
Section 2	Experimental Synthetic Procedures	page S4–S5
Section 3	¹ H and ¹³ C NMR Spectra of Final Compounds	page S6–S13
Section 4	Break Junction Experiments	page S14–S17
Section 5	Computational Methods	page S18–S20
Section 6	Tight binding models	pages S21
Section 7	Frontier Orbitals	pages S21–S22
Section 8	Reference	page 23

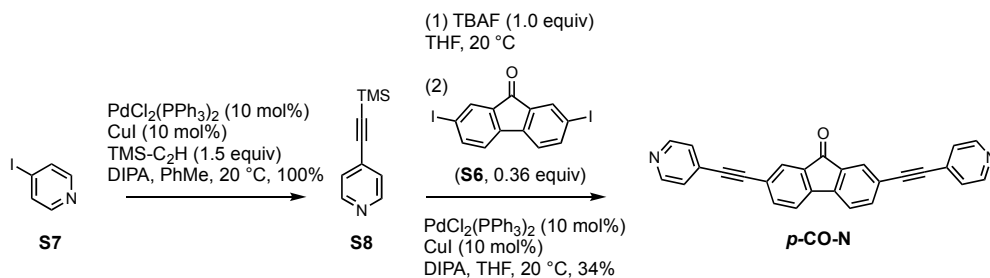
Section 1. Synthetic Schemes



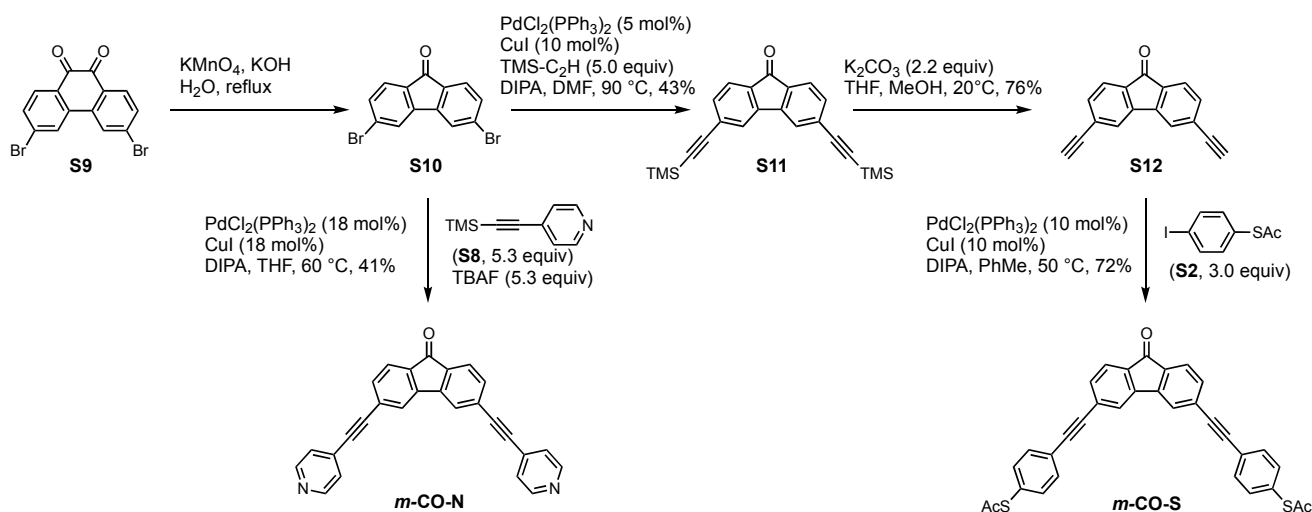
Scheme S1. Preparation of intermediate **S4** was carried out as described in Ref. 1–3.



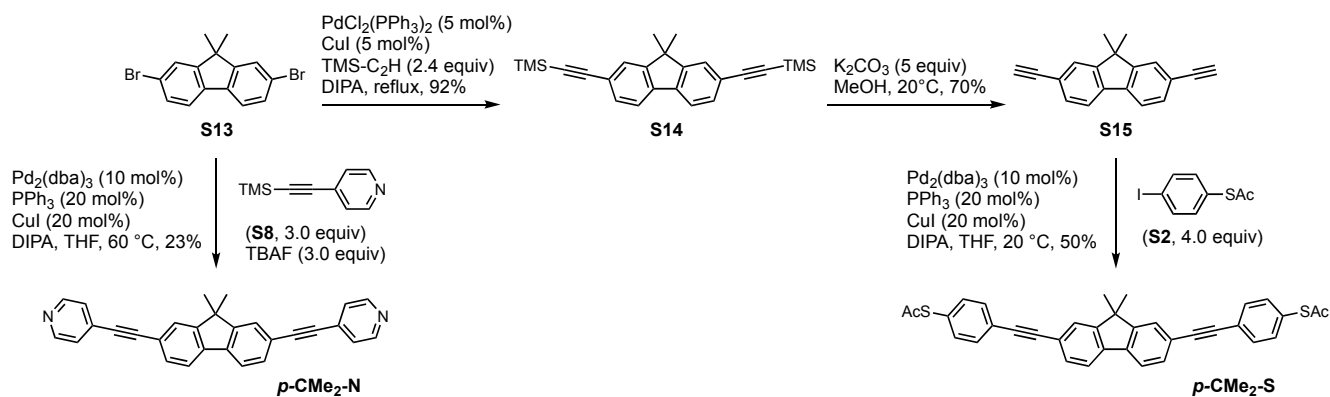
Scheme S2. Preparation of intermediate **S6** was carried out as described in Ref. 4, 5. The synthesis of *p*-CO-S via a different route was reported in Ref. 6.



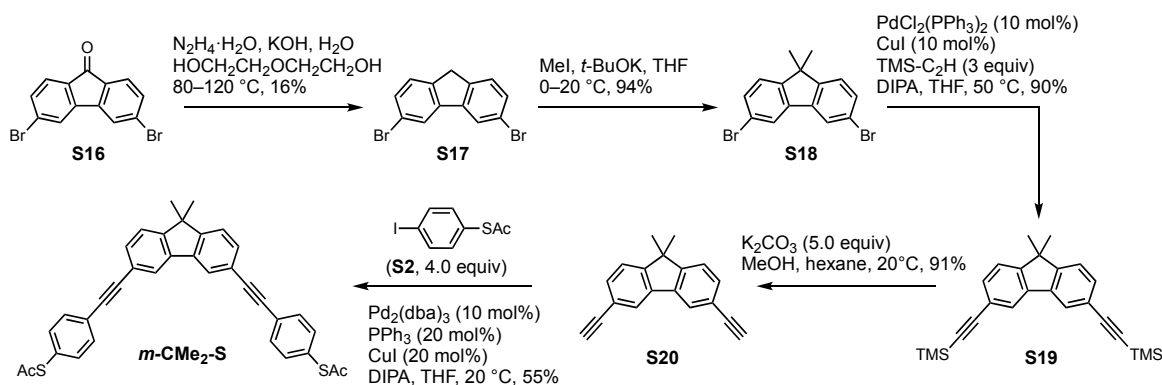
Scheme S3. Preparation of intermediate **S8** was carried out as described in Ref. 7.



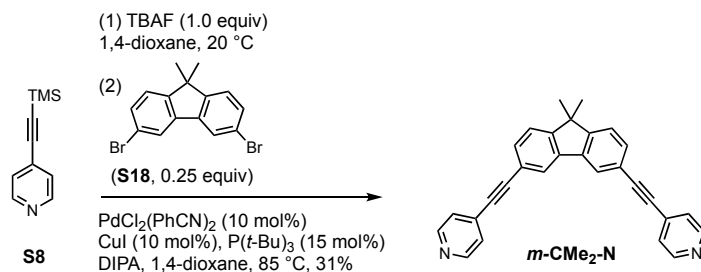
Scheme S4. Preparation of intermediate **S10** was carried out as described in Ref. 5, 8, 9. Conversion of **S10** to **S12** was carried out as described in Ref. 10.



Scheme S5. Preparation of intermediate **S15** was carried out as described in Ref. 11. The synthesis of *p*-CMe₂-N was carried out using a similar procedure to that reported in Ref. 12. The synthesis of a closely related compound to *p*-CMe₂-S was reported in Ref. 13.



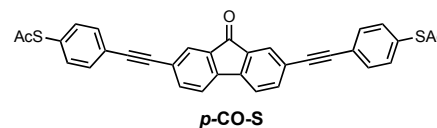
Scheme S6. Preparation of intermediate **S18** was carried out as described in Ref. 8, 9.



Scheme S7. The synthesis of *m*-CMe₂-N was carried out using a similar procedure to that reported in Ref. 12.

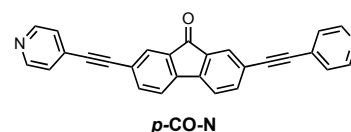
Section 2. Experimental Synthetic Procedures

Synthesis of *p*-CO-S. A 20 mL flask charged with 2,7-diiodofluorenone **S6** (108 mg, 0.25 mmol, 1.0 eq.), 4-ethynyl-1-thioacetylbenzene **S4** (92 mg, 0.52 mmol, 2.1 eq.), PdCl₂(PPh₃)₂ (17 mg, 0.025 mmol, 0.1 eq.), CuI (4.8 mg, 0.025 mmol, 0.1 eq.) was flushed with nitrogen. Diisopropylamine (DIPA, 1 mL) and THF (5 mL) were then added. After being stirred at 50 °C for 1.5 h, the reaction was quenched with water (10 mL). The product was extracted with CHCl₃ (10 mL × 3), washed with brine, and dried over Na₂SO₄. Purification by chromatography on silica gel (CHCl₃) provided ***p*-CO-S** as a yellow solid (88 mg, 67%). For conductance measurement, high purity sample was obtained by reprecipitation from CHCl₃ and hexane.



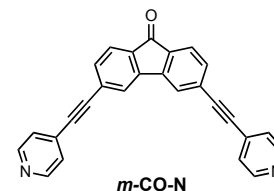
¹H NMR (500 MHz, CDCl₃) δ 2.45 (s, 6H), 7.42 (d, *J* = 8.0 Hz, 4H), 7.53–7.58 (m, 6H), 7.67 (dd, *J* = 8.0 Hz, 1.5 Hz, 2H), 7.82 (d, *J* = 1.5 Hz, 2H); ¹³C NMR (125 MHz, CDCl₃) δ 30.47, 90.27, 90.84, 120.84, 124.10, 124.37, 127.69, 128.72, 132.38, 134.42, 134.62, 138.09, 143.56, 192.24, 193.50; HRMS (ESI) *m/z*: calculated for [C₃₃H₂₁O₃S₂]⁺: 529.0927, found: 529.0923 Data match those reported in Ref. 6.

Synthesis of *p*-CO-N. Under an atmosphere of N₂, 4-(trimethylsilylethynyl)pyridine **S8** (0.12 g, 0.70 mmol, 2.8 eq.) was dissolved in THF (2 mL). A solution of TBAF (1.0 M in THF, 0.7 mL, 0.70 mmol, 2.8 eq.) was added at room temperature and stirred for 30 min. In the other Schlenk flask charged with 2,7-diiodofluorenone **S6** (0.11 g, 0.25 mmol, 1.0 eq.), PdCl₂(PPh₃)₂ (17.5 mg, 0.025 mmol, 0.1 eq.), CuI (4.8 mg, 0.025 mmol, 0.1 eq.) was flushed with nitrogen. DIPA (1 mL), THF (3 mL) and the solution of 4-ethynylpyridine prepared above were then added. After stirring at room temperature for 12 h, the reaction mixture was filtrated over short plug of silica gel, washed with CH₂Cl₂ containing 5% Et₃N and evaporated. Purification by chromatography on silica gel (CHCl₃/Et₃N = 20/1) and reprecipitation from CHCl₃/hexane provided ***p*-CO-N** as a yellow powder (33 mg, 34%).



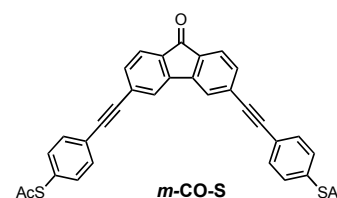
¹H NMR (500 MHz, CDCl₃) δ 7.40 (dd, *J* = 1.5, 4.5 Hz, 4H), 7.59 (dd, *J* = 0.5, 8.0 Hz, 2H), 7.72 (dd, *J* = 1.5, 8.0 Hz, 2H), 7.86 (dd, *J* = 0.5, 1.5 Hz, 2H), 8.63 (dd, *J* = 1.5, 4.5 Hz, 4H); ¹³C NMR (125 MHz, CDCl₃) δ 88.80, 92.87, 121.05, 123.72, 125.66, 127.93, 130.99, 134.66, 138.40, 144.00, 150.04, 191.84; HRMS (ESI) *m/z*: calculated for [C₂₇H₁₅ON₂]⁺: 383.1179, found: 383.1179.

Synthesis of *m*-CO-N. In Schlenk flask charged with 3,6-dibromofluorenone **S10** (44 mg, 0.072 mmol, 1.0 eq.), 4-(trimethylsilylethynyl)pyridine **S8** (67 mg, 0.38 mmol, 5.3 eq.), PdCl₂(PPh₃)₂ (9.1 mg, 0.013 mmol, 0.18 eq.), CuI (2.5 mg, 0.013 mmol, 0.18 eq.) was flushed with nitrogen. A solution of TBAF (1.0 M in THF, 0.38 mL, 0.38 mmol, 5.3 eq.), DIPA (2 mL) and THF (2 mL) were added. After stirring at 60 °C for 12 h, the reaction mixture was filtrated over short plug of silica gel, washed with CH₂Cl₂ containing 5% Et₃N and evaporated. Purification by chromatography on silica gel (hexane/EtOAc/Et₃N = 10/50/1) and reprecipitation from CHCl₃/hexane provided ***m*-CO-N** as a yellow powder (11 mg, 41%).



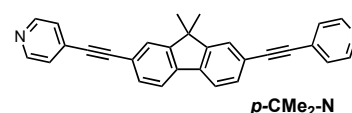
¹H NMR (500 MHz, CDCl₃) δ 7.42 (dd, *J* = 1.5, 4.5 Hz, 4H), 7.54 (dd, *J* = 1.0, 3.0 Hz, 2H), 7.72 (d, *J* = 3.0 Hz, 2H), 7.74 (d, *J* = 1.0 Hz, 2H), 8.67 (dd, *J* = 1.5, 4.5 Hz, 4H); ¹³C NMR (125 MHz, CDCl₃) δ 90.19, 93.03, 123.84, 124.71, 125.71, 128.75, 130.76, 133.41, 134.43, 143.79, 150.12, 191.79; HRMS (ESI) *m/z*: calculated for [C₂₇H₁₅ON₂]⁺: 383.1179, found: 383.1180.

Synthesis of *m*-CO-S. A 20 mL flask charged with 3,6-diethynylfluorenone **S12** (30 mg, 0.13 mmol, 1.0 eq.), 4-iodo-1-thioacetylbenzene **S2** (108 mg, 0.39 mmol, 3.0 eq.), PdCl₂(PPh₃)₂ (9.1 mg, 0.013 mmol, 0.1 eq.), CuI (2.5 mg, 0.013 mmol, 0.1 eq.) was flushed with nitrogen. DIPA (4 mL) and toluene (4 mL) were then added. After stirring at 50 °C for 3 h, the reaction was quenched with water (10 mL). The product was extracted with CHCl₃ (10 mL × 3), washed with brine, and dried over Na₂SO₄. Purification by chromatography on silica gel (CHCl₃/petrol ether = 1/1 and then CHCl₃) provided ***m*-CO-S** as an orange solid (35 mg, 72%). For conductance measurement, high purity sample was obtained by reprecipitation from CHCl₃ and hexane.



¹H NMR (500 MHz, CDCl₃) δ 2.45 (s, 6H), 7.44 (d, *J* = 8.5 Hz, 4H), 7.49 (dd, *J* = 7.5 Hz, 1.5 Hz, 2H), 7.59 (d, *J* = 8.5 Hz, 4H), 7.68 (dd, *J* = 7.5 Hz, 0.5 Hz, 2H), 7.71 (d, *J* = 1.5 Hz, 2H); ¹³C NMR (125 MHz, CDCl₃) δ 30.49, 90.59, 92.51, 123.65, 123.85, 124.54, 129.11, 129.59, 132.48, 132.99, 133.98, 134.45, 143.85, 192.03, 193.40 HRMS (ESI) *m/z*: calculated for [C₃₃H₂₁O₃S₂]⁺: 529.0927, found: 529.0926.

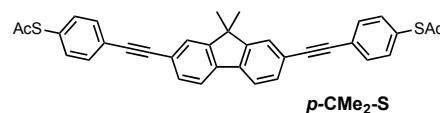
Synthesis of *p*-CMe₂-N. A Schlenk flask charged with 2,7-dibromo-9,9-dimethylfluorene **S13** (176 mg, 0.50 mmol, 1.0 eq.), Pd₂(dba)₃ (46 mg, 0.050 mmol, 0.1 eq.), PPh₃ (26 mg, 0.10 mmol, 0.2 eq.)



and CuI (19 mg, 0.10 mmol, 0.2 eq.) was flushed with nitrogen. THF (6 mL), DIPA (2 mL) and 4-(trimethylsilylethynyl)pyridine **S8** (263 mg, 1.50 mmol, 3.0 eq.) were then added. TBAF (1.0 M in THF, 1.5 mL, 1.50 mmol, 3.0 eq.) was slowly added to the mixture without light. After stirring at 60 °C without light for 12 h, the reaction mixture was filtrated over short plug of silica gel, washed with CHCl₃ containing 5% Et₃N and evaporated. Purification by chromatography on silica gel (toluene/EtOAc = 5/1 + 5 vol% Et₃N) provided **p-CMe₂-N** as a light brown powder (46 mg, 23%).

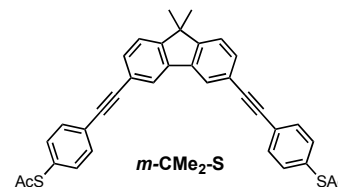
¹H NMR (500 MHz, CDCl₃) δ 1.53 (s, 6H), 7.41 (dd, *J* = 1.5, 4.5 Hz, 4H), 7.57 (dd, *J* = 1.5, 8.0 Hz, 2H), 7.64 (d, *J* = 1.5 Hz, 2H), 7.74 (d, *J* = 7.5 Hz, 2H), 8.62 (dd, *J* = 1.5, 4.5 Hz, 4H); ¹³C NMR (125 MHz, CDCl₃) δ 27.04, 47.19, 87.37, 94.82, 120.71, 121.39, 125.65, 126.45, 131.44, 131.64, 139.54, 149.95, 154.25; HRMS (ESI) *m/z*: calculated for [C₂₉H₂₁N₂]⁺: 397.1699, found: 397.1697. Data match those reported in Ref. 12.

Synthesis of p-CMe₂-S. Under N₂ atmosphere, to a solution of 2,7-diethynyl-9,9-dimethylfluorene **S15** (48 mg, 0.20 mmol, 1.0 eq.), 4-acetylthio-1-iodobenzene **S2** (0.22 g, 0.80 mmol, 4.0 eq.), Pd₂(dba)₃ (18 mg, 0.020 mmol, 0.1 eq.), PPh₃ (10 mg, 0.040 mmol, 0.2 eq.), CuI (7.6 mg, 0.040 mmol, 0.2 eq.) in THF (5 mL) was added DIPA (1 mL). After stirring at room temperature for 12 h, the reaction mixture was filtrated over short plug of silica gel, washed with CHCl₃ and evaporated. Purification by chromatography on silica gel (petrol ether /CH₂Cl₂ = 1/1) and recrystallization from toluene/hexane (1/1 vol. %) provided **p-CMe₂-S** as a white powder (54 mg, 50%).



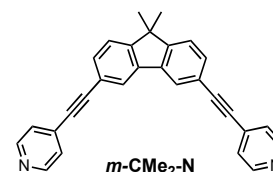
¹H NMR (500 MHz, CDCl₃) δ 1.53 (s, 6H), 2.45 (s, 6H), 7.41–7.43 (m, 4H), 7.54 (dd, *J* = 1.5, 8.0 Hz, 2H), 7.57–7.59 (m, 4H), 7.61 (d, *J* = 1.0 Hz, 2H), 7.70 (dd, *J* = 1.0, 8.0 Hz, 2H); ¹³C NMR (125 MHz, CDCl₃) δ 27.08, 30.44, 47.11, 89.26, 91.98, 120.49, 122.02, 124.75, 126.19, 128.13, 131.15, 132.30, 134.39, 139.07, 154.14, 193.66; HRMS (ESI) *m/z*: calculated for [C₃₅H₂₇O₂S₂]⁺: 543.1447, found: 543.1447.

Synthesis of m-CMe₂-S. Under N₂ atmosphere, to a solution of 3,6-diethynyl-9,9-dimethylfluorene **S20** (60 mg, 0.25 mmol, 1.0 eq.), 4-acetylthio-1-iodobenzene **S2** (0.28 g, 1.0 mmol, 4.0 eq.), Pd₂(dba)₃ (23 mg, 0.025 mmol, 0.1 eq.), PPh₃ (13 mg, 0.050 mmol, 0.2 eq.), CuI (9.5 mg, 0.050 mmol, 0.2 eq.) in THF (5 mL) was added DIPA (1 mL). After stirring at room temperature for 12 h, the reaction mixture was filtrated over short plug of silica gel, washed with CH₂Cl₂ and evaporated. Purification by chromatography on silica gel (hexane/CH₂Cl₂ = 1/1) provided **m-CMe₂-S** as a white powder (75 mg, 55%). For conductance measurement, high purity sample was obtained by recrystallization from toluene/hexane (1/5 vol. %).



¹H NMR (500 MHz, CDCl₃) δ 1.50 (s, 6H), 2.44 (s, 6H), 7.41–7.43 (m, 6H), 7.52 (dd, *J* = 1.5, 8.0 Hz, 2H), 7.59 (dt, *J* = 2.0, 8.5 Hz, 4H), 7.91 (d, *J* = 1.5 Hz, 2H); ¹³C NMR (125 MHz, CDCl₃) δ 27.04, 30.45, 47.37, 88.43, 91.52, 121.86, 122.90, 123.58, 124.82, 128.09, 131.41, 132.35, 134.40, 138.82, 154.26, 193.69; HRMS (ESI) *m/z*: calculated for [C₃₅H₂₇O₂S₂Na]⁺: 565.1266, found: 565.1265.

Synthesis of m-CMe₂-N. In N₂ atmosphere, 4-(trimethylsilylethynyl)pyridine **S8** (0.14 g, 0.80 mmol, 4.0 eq.) was dissolved in 1,4-dioxane (1 mL). A solution of TBAF (1.0 M in THF, 0.8 mL, 0.80 mmol, 4.0 eq.) was added at room temperature and stirred for 30 min without light. In the other Schlenk flask charged with 3,6-dibromo-9,9-dimethylfluorene **S18** (70 mg, 0.20 mmol, 1.0 eq.), PdCl₂(PhCN)₂ (7.7 mg, 0.020 mmol, 0.1 eq.), CuI (3.8 mg, 0.020 mmol, 0.1 eq.) and 0.2 M P(*t*-Bu)₃ solution in toluene (0.15 mL, 0.030 mmol, 0.15 eq.) was flushed with nitrogen. DIPA (1 mL), 1,4-dioxane (1 mL) and the solution of 4-ethynylpyridine prepared above were then added. After stirring at 85 °C for 3 h, the reaction mixture was filtrated over short plug of silica gel, washed with CHCl₃ containing 5% Et₃N and concentrated. Purification by chromatography on silica gel twice (toluene/EtOAc = 5/1 + 5 vol. % Et₃N and CHCl₃/Et₃N = 20/1) provided **m-CMe₂-N** as a light yellow powder (25 mg, 31%).



¹H NMR (400 MHz, CDCl₃) δ 1.51 (s, 6H), 7.41 (dd, *J* = 1.5, 4.5 Hz, 4H), 7.46 (d, *J* = 8.0 Hz, 2H), 7.51 (dd, *J* = 1.5, 8.0 Hz, 2H), 7.93 (d, *J* = 1.5 Hz, 2H), 8.62 (dd, *J* = 1.5, 4.5 Hz, 4H); ¹³C NMR (125 MHz, CDCl₃) δ 26.97, 47.53, 86.57, 94.38, 121.12, 123.09, 123.80, 125.70, 131.67, 131.74, 138.76, 149.95, 154.90; HRMS (ESI) *m/z*: calculated for [C₂₉H₂₁N₂]⁺: 397.1699, found: 397.1698. Data match those reported in Ref. 12.

Section 3. ^1H and ^{13}C NMR Spectra of Final Compounds

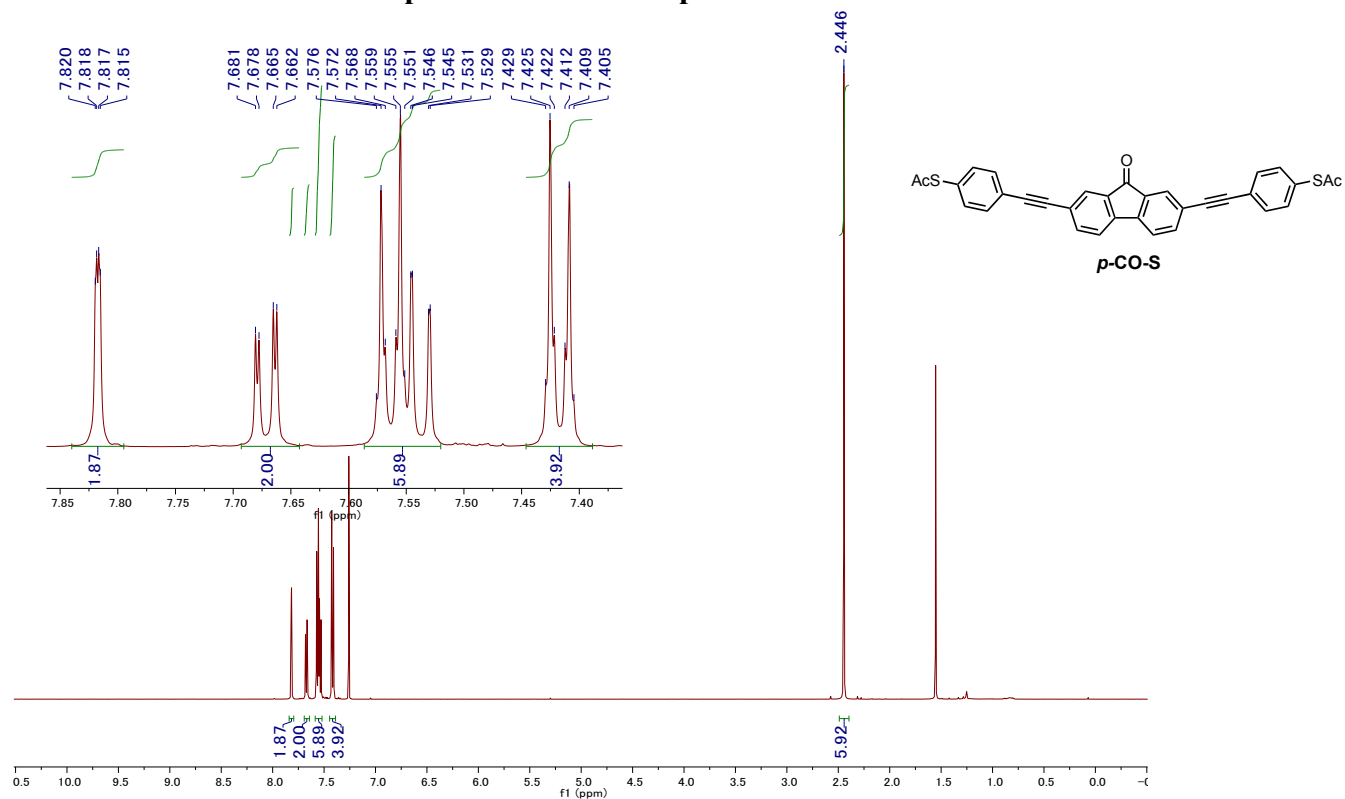


Figure S3.1. ^1H NMR spectrum of *p*-CO-S (500 MHz, CDCl_3)

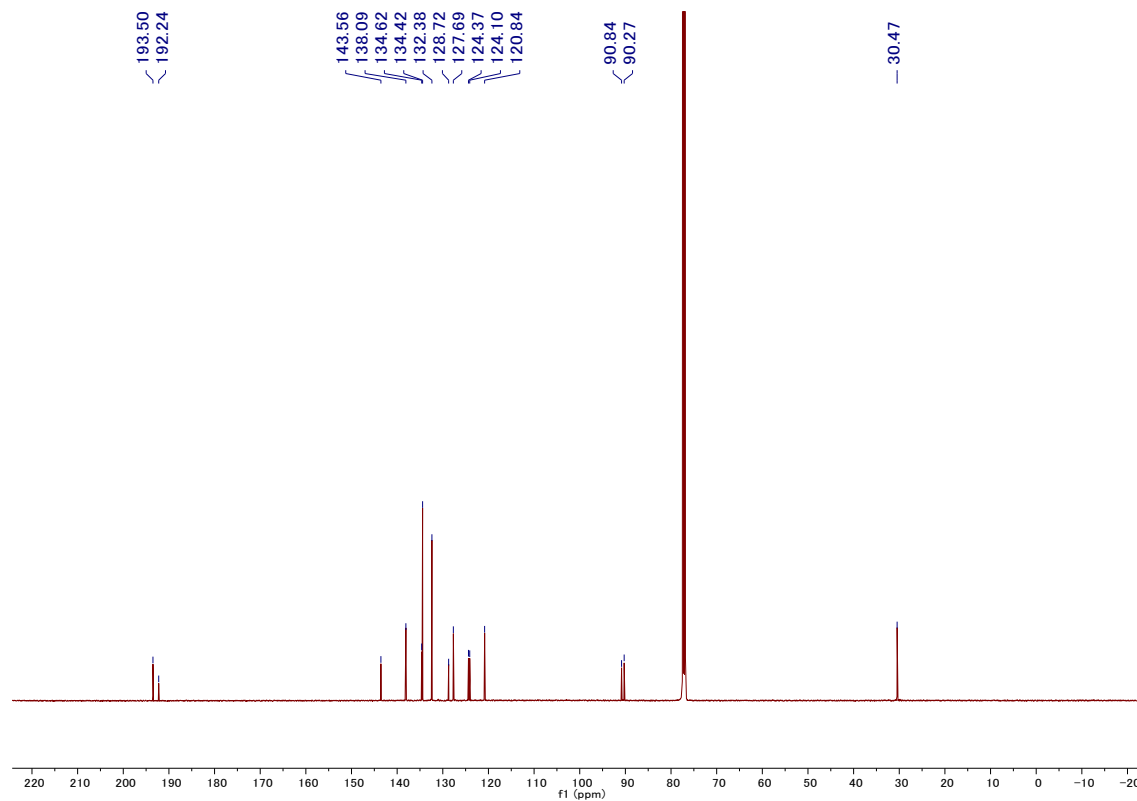


Figure S3.2. ^{13}C -NMR spectrum of *p*-CO-S (125 MHz, CDCl_3)

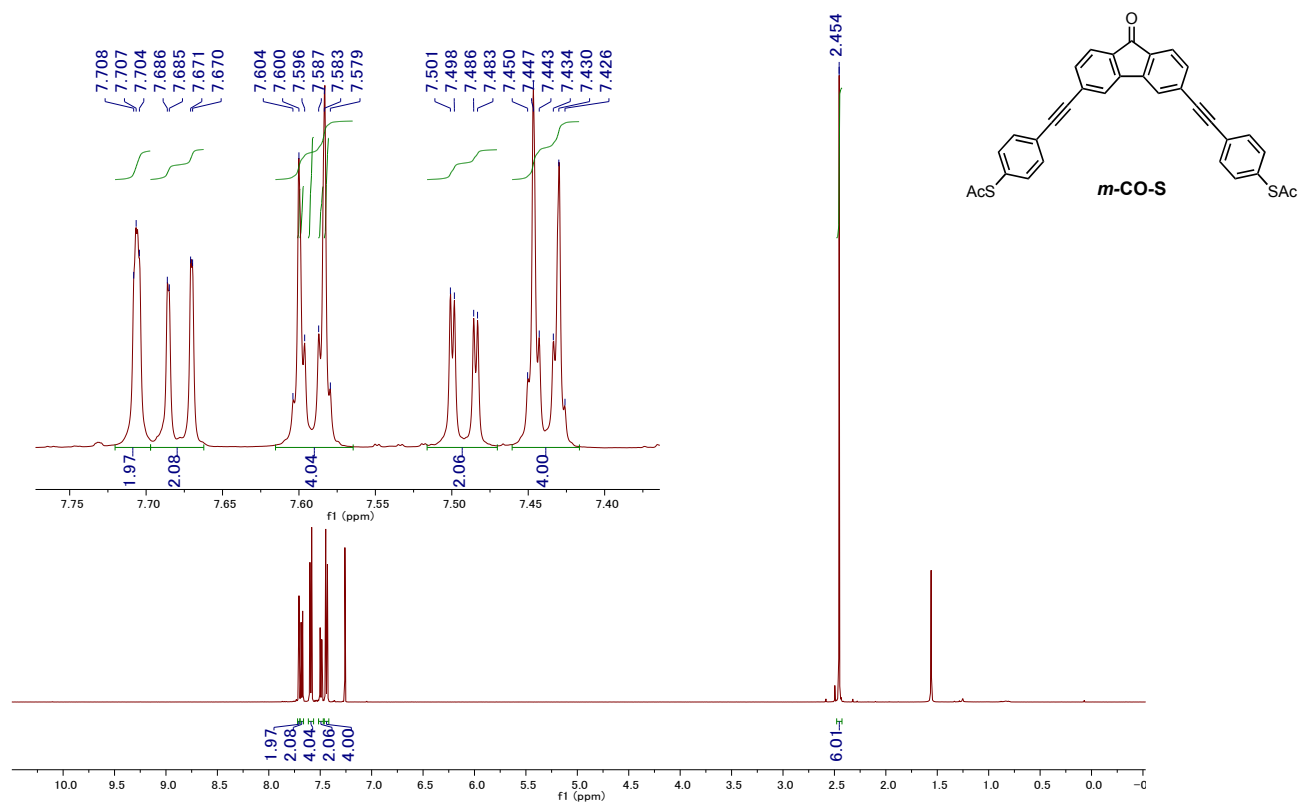


Figure S3.3. ¹H-NMR spectrum of *m*-CO-S (500 MHz, CDCl₃)

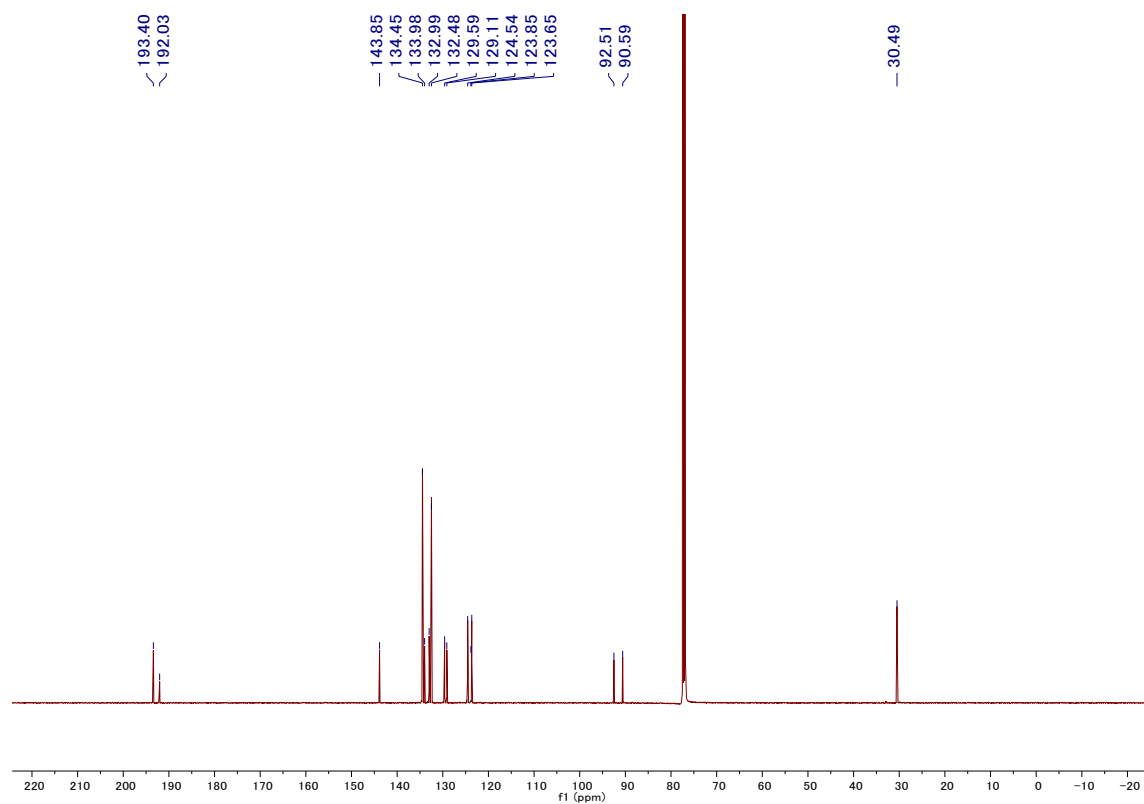


Figure S3.4. ¹³C-NMR spectrum of *m*-CO-S (125 MHz, CDCl₃)

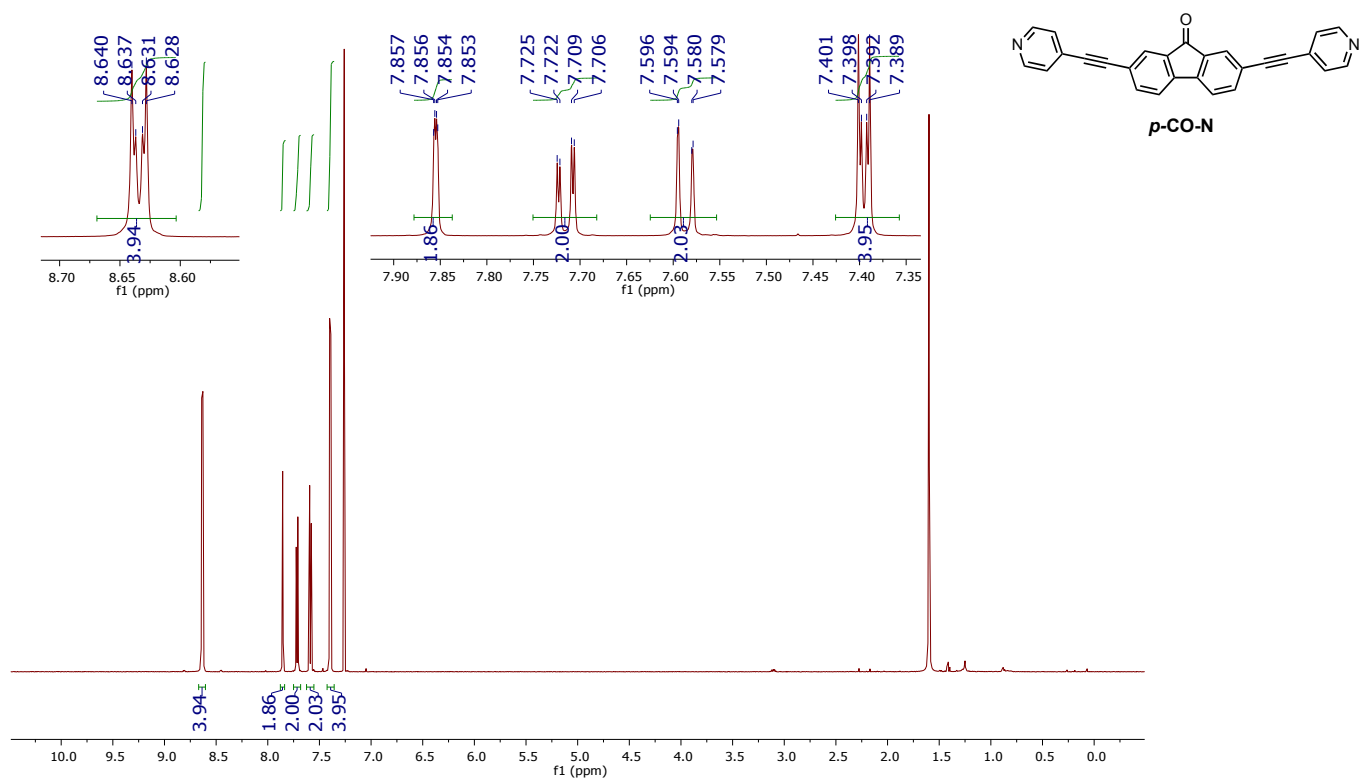


Figure S3.5. ¹H-NMR spectrum of *p*-CO-N (500 MHz, CDCl₃)

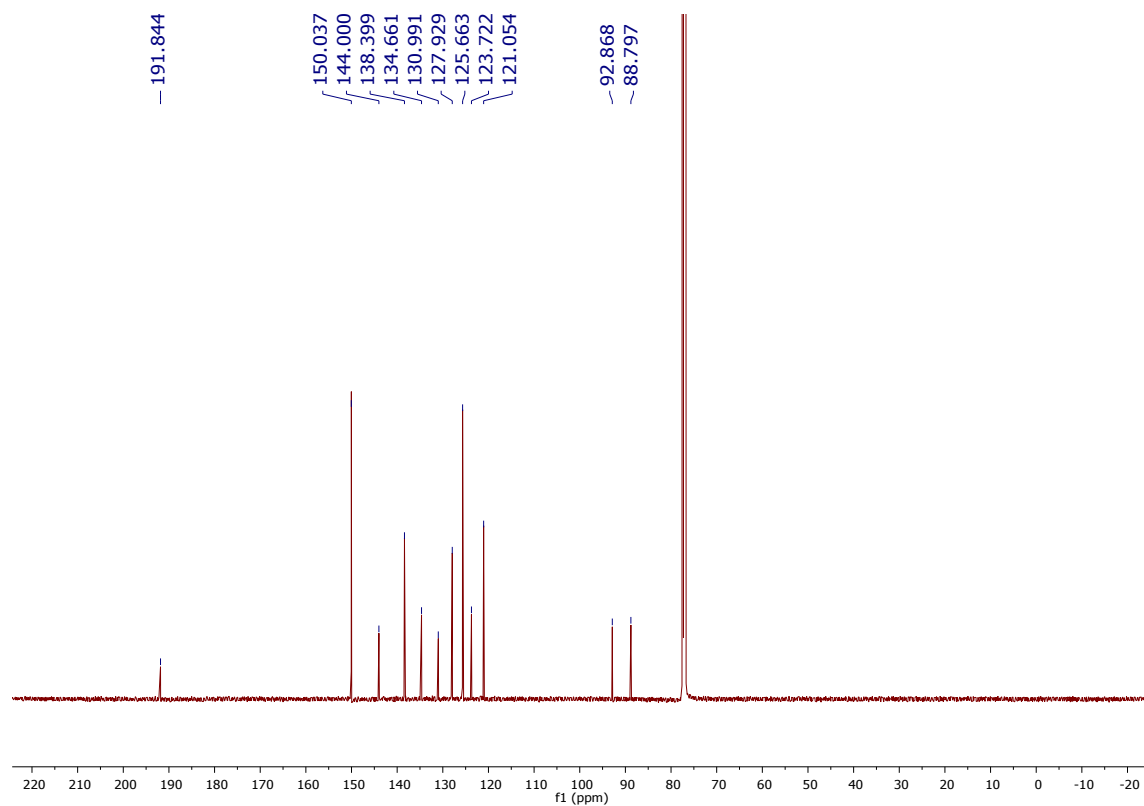


Figure S3.6. ¹³C-NMR spectrum of *p*-CO-N (125 MHz, CDCl₃)

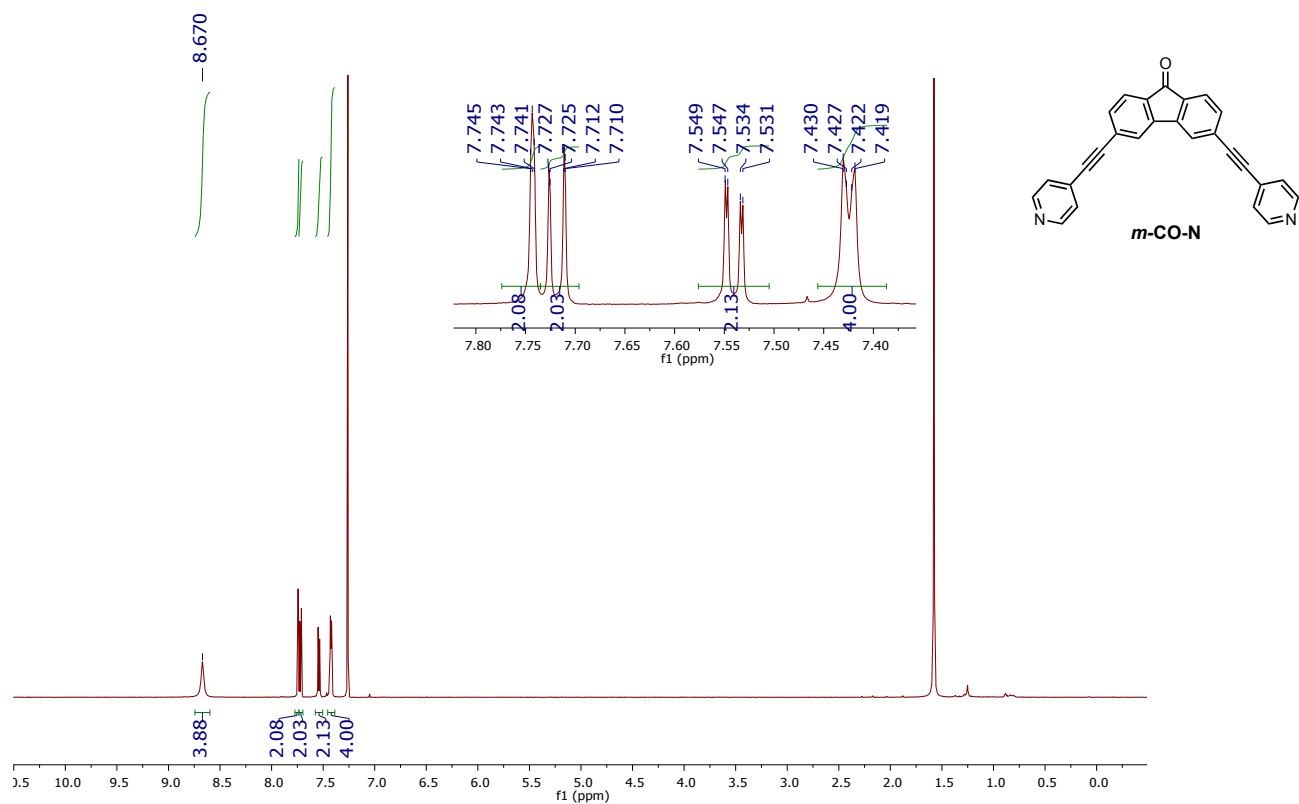


Figure S3.7. ¹H-NMR spectrum of *m*-CO-N (500 MHz, CDCl₃)

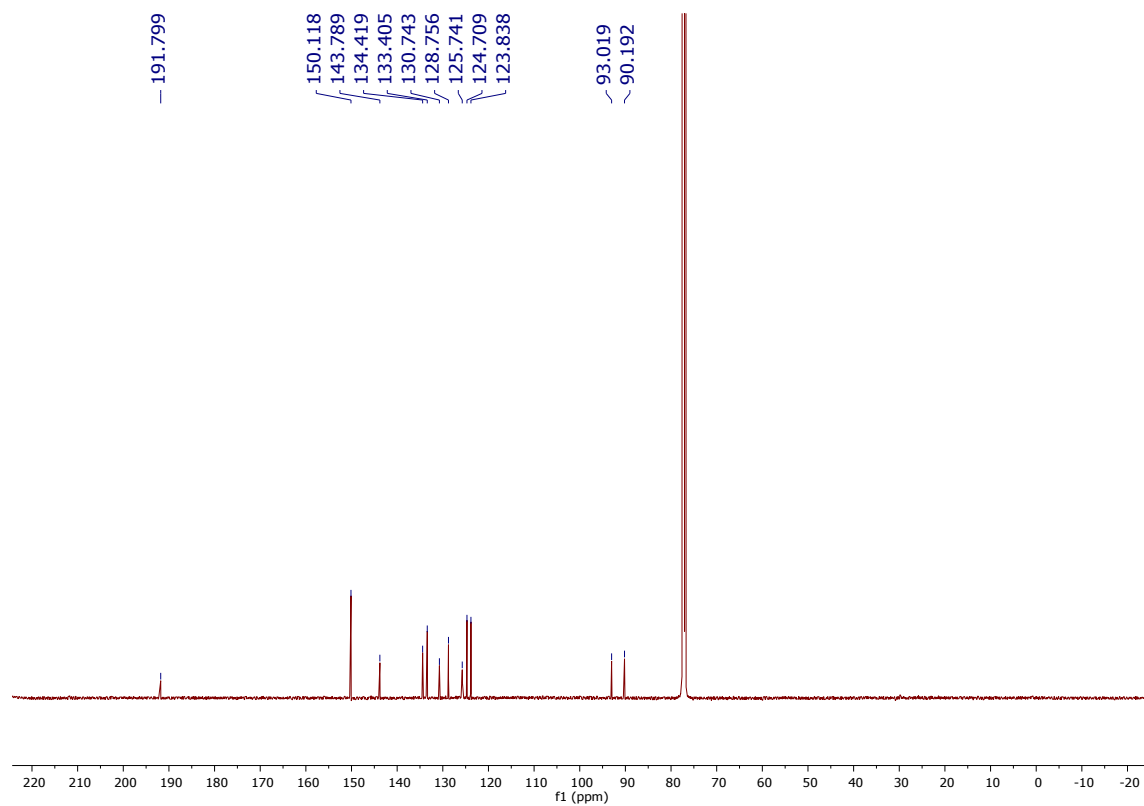


Figure S3.8. ¹³C-NMR spectrum of *m*-CO-N (125 MHz, CDCl₃)

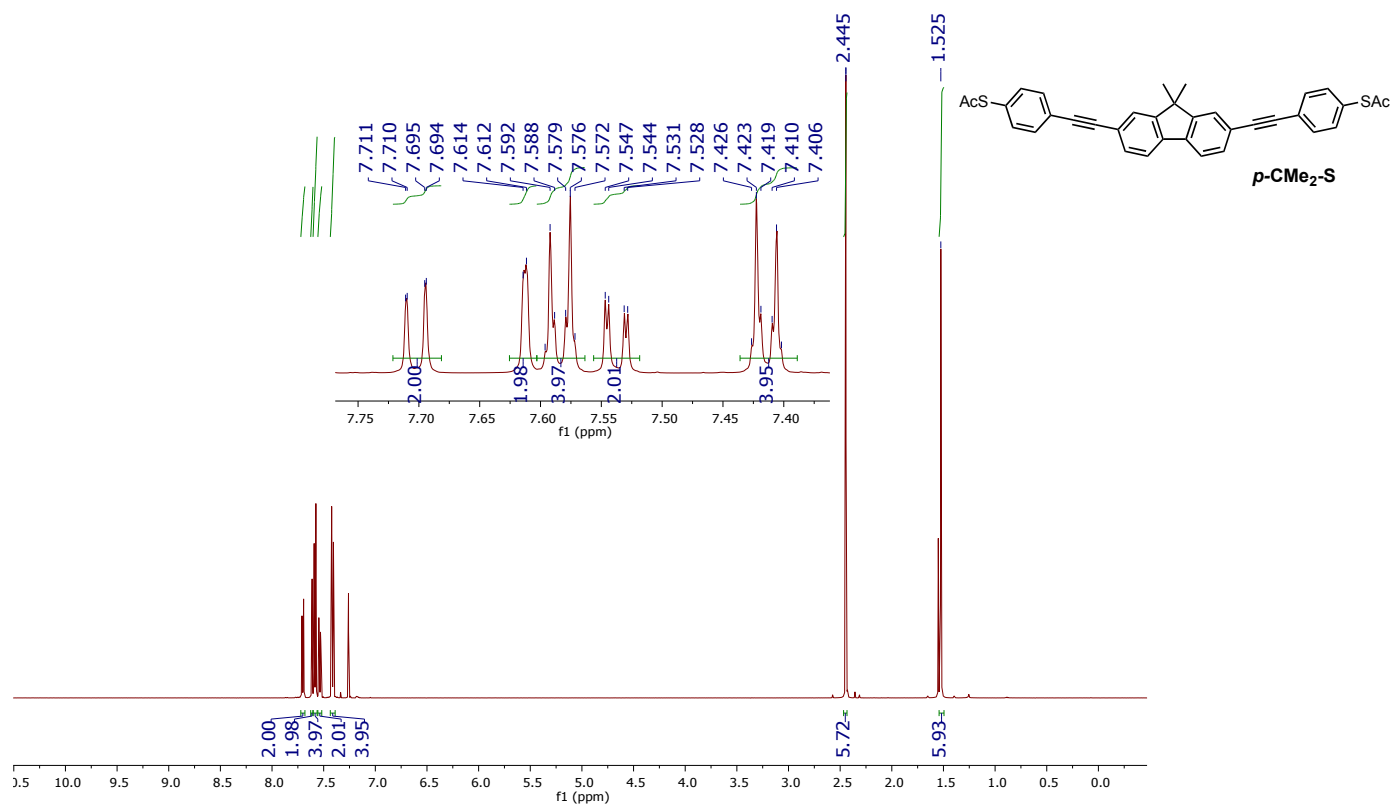


Figure S3.9. ¹H-NMR spectrum of *p*-CMe₂-S (500 MHz, CDCl₃)

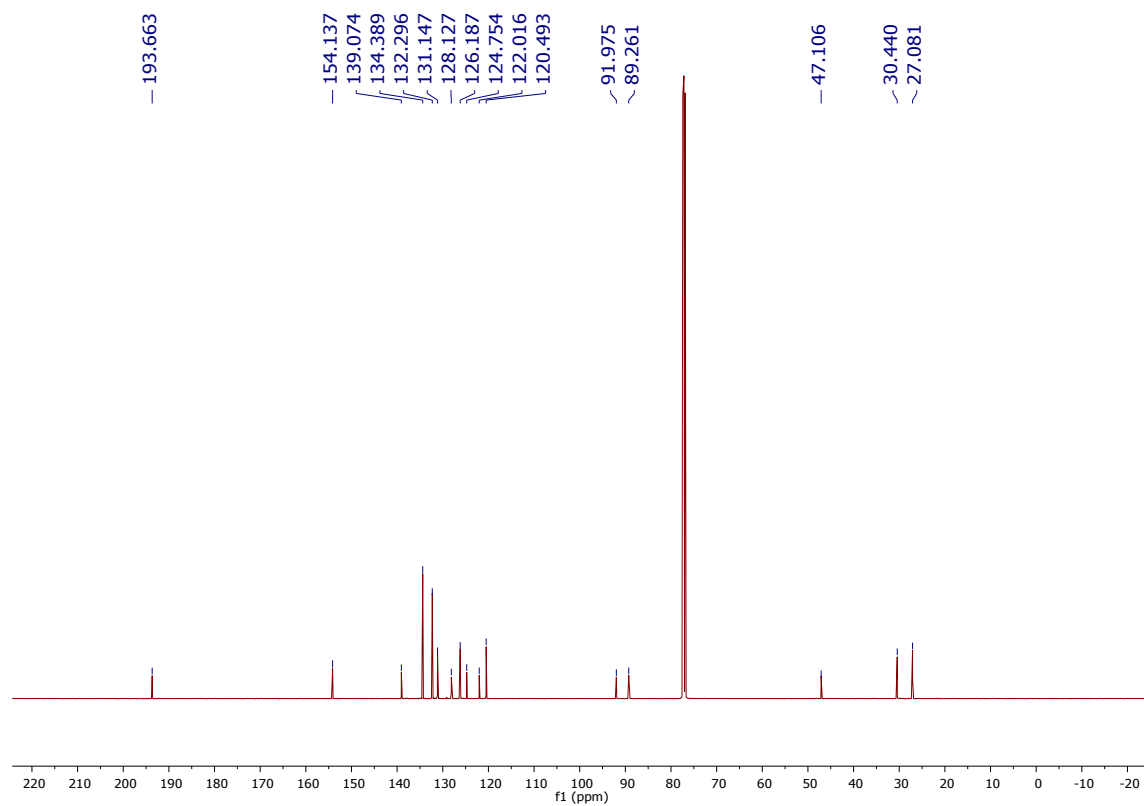


Figure S3.10. ¹³C-NMR spectrum of *p*-CMe₂-S (125 MHz, CDCl₃)

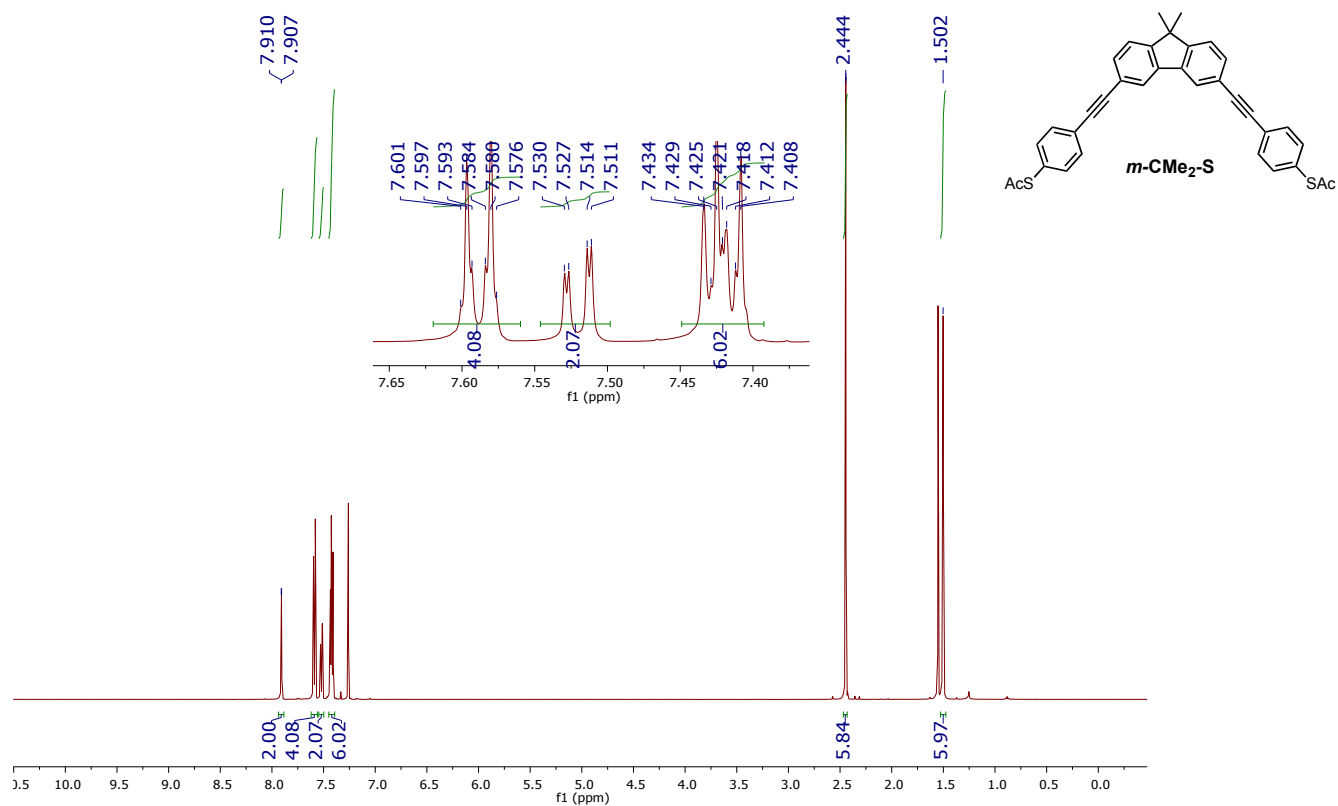


Figure S3.11. ¹H-NMR spectrum of *m*-CMe₂-S (500 MHz, CDCl₃)

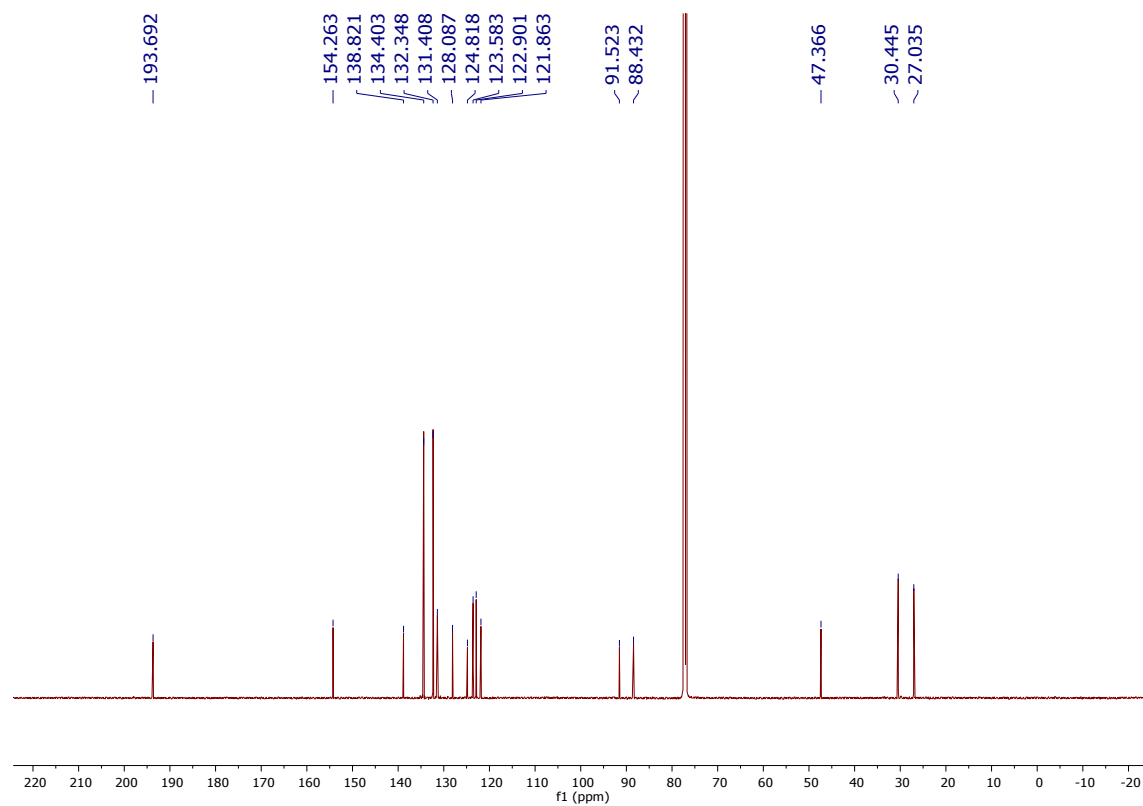


Figure S3.12. ¹³C-NMR spectrum of *m*-CMe₂-S (125 MHz, CDCl₃)

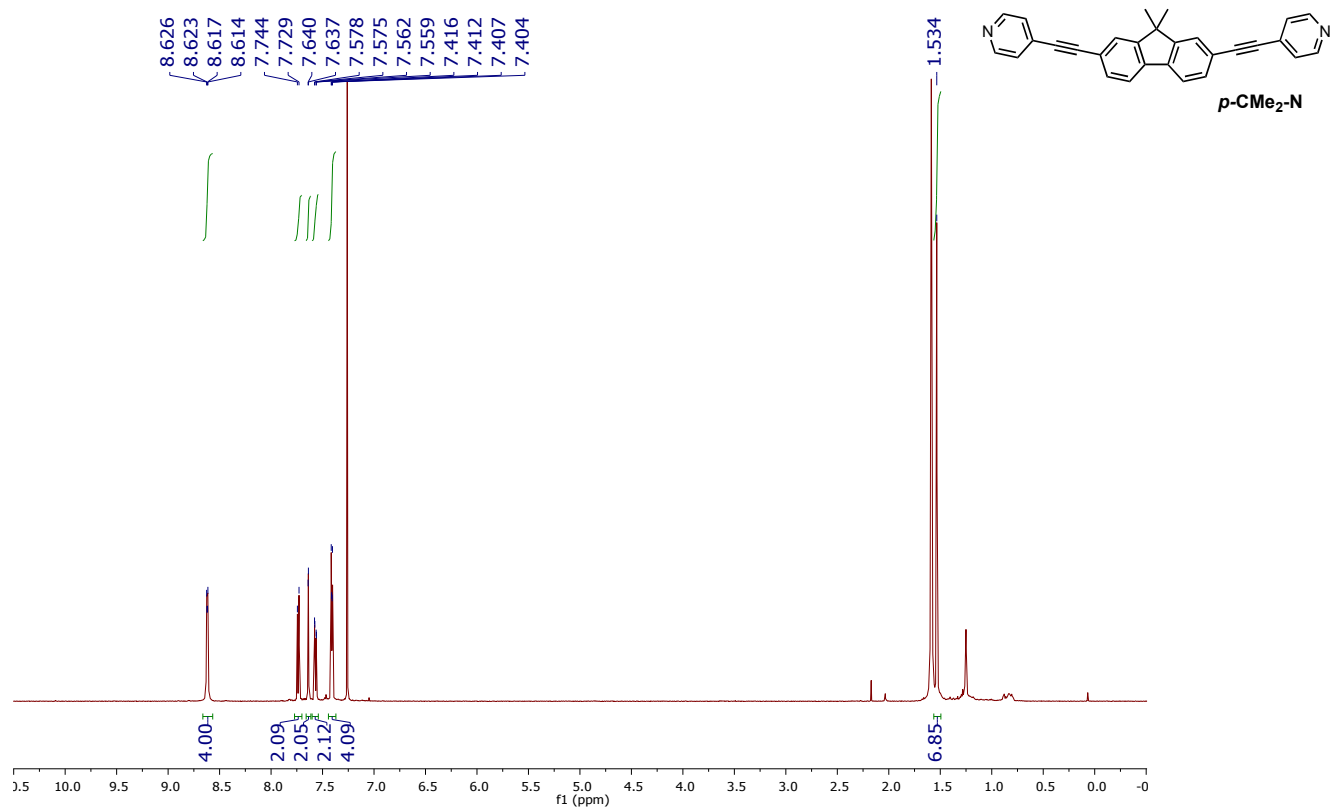


Figure S3.13. ¹H-NMR spectrum of *p*-CMe₂-N (500 MHz, CDCl₃)

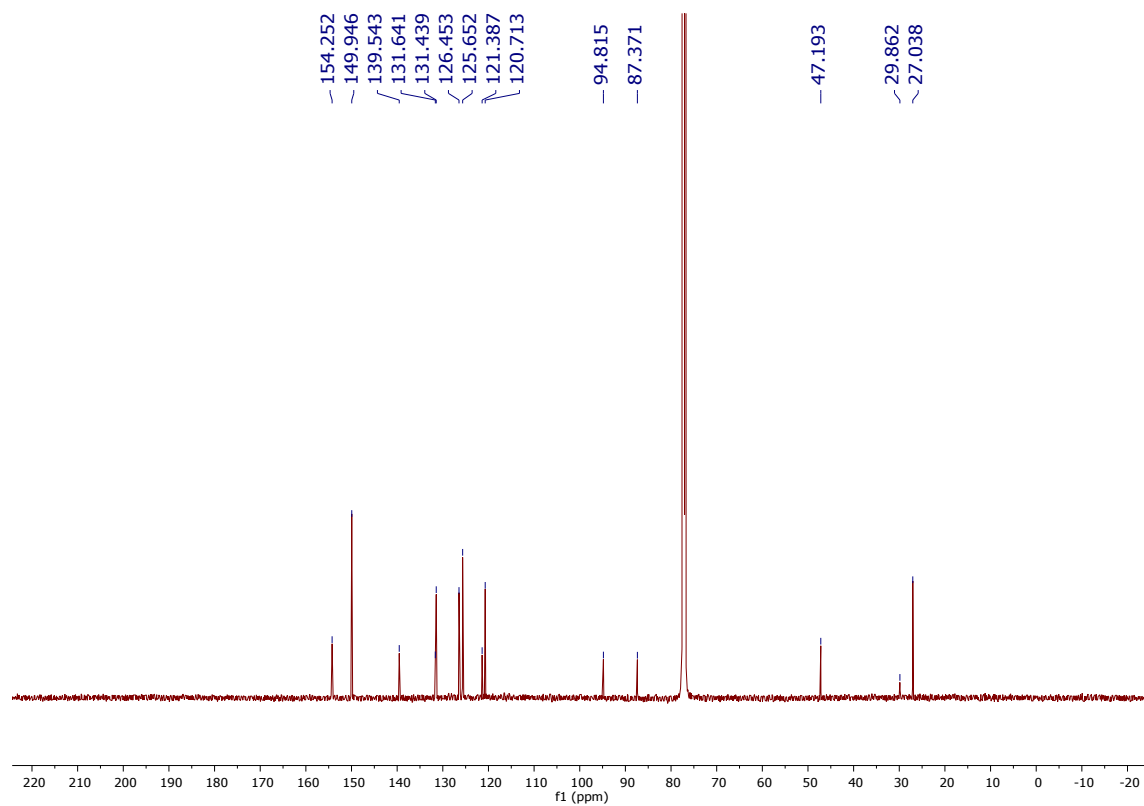


Figure S3.14. ¹³C-NMR spectrum of *p*-CMe₂-N (125 MHz, CDCl₃)

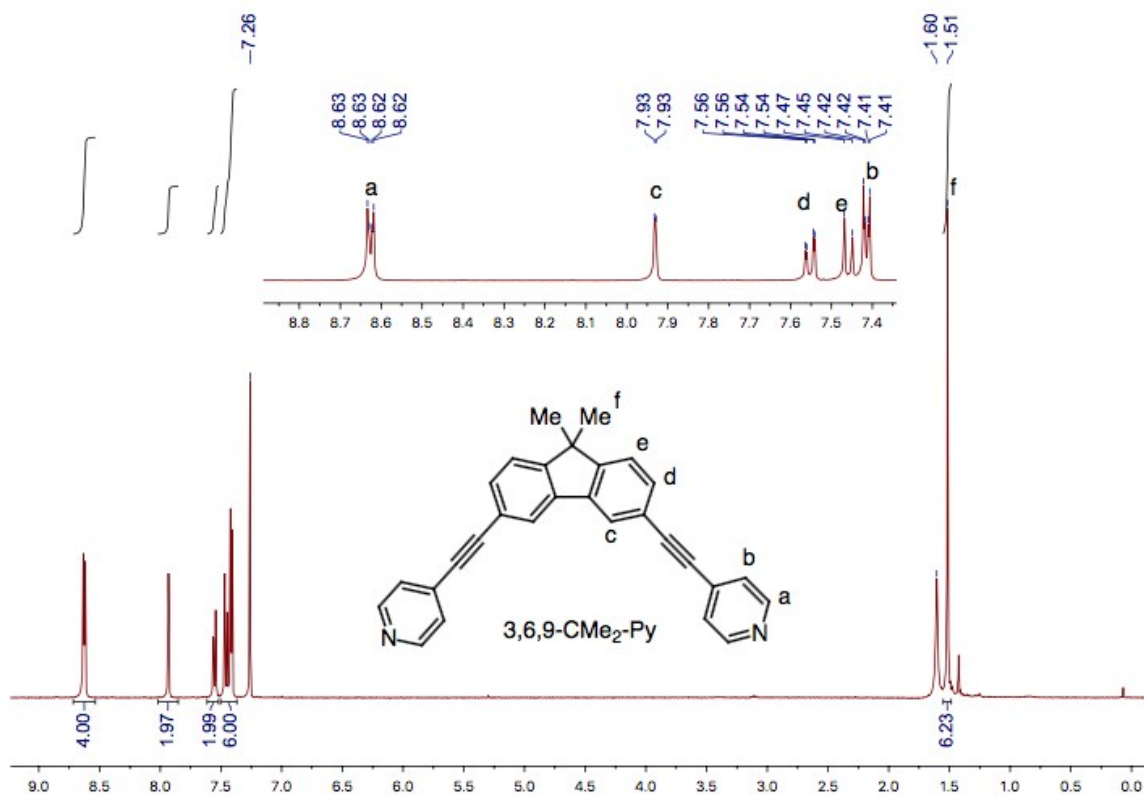


Figure S3.15. ^1H -NMR spectrum of *m*- $\text{CMe}_2\text{-N}$ (500 MHz, CDCl_3)

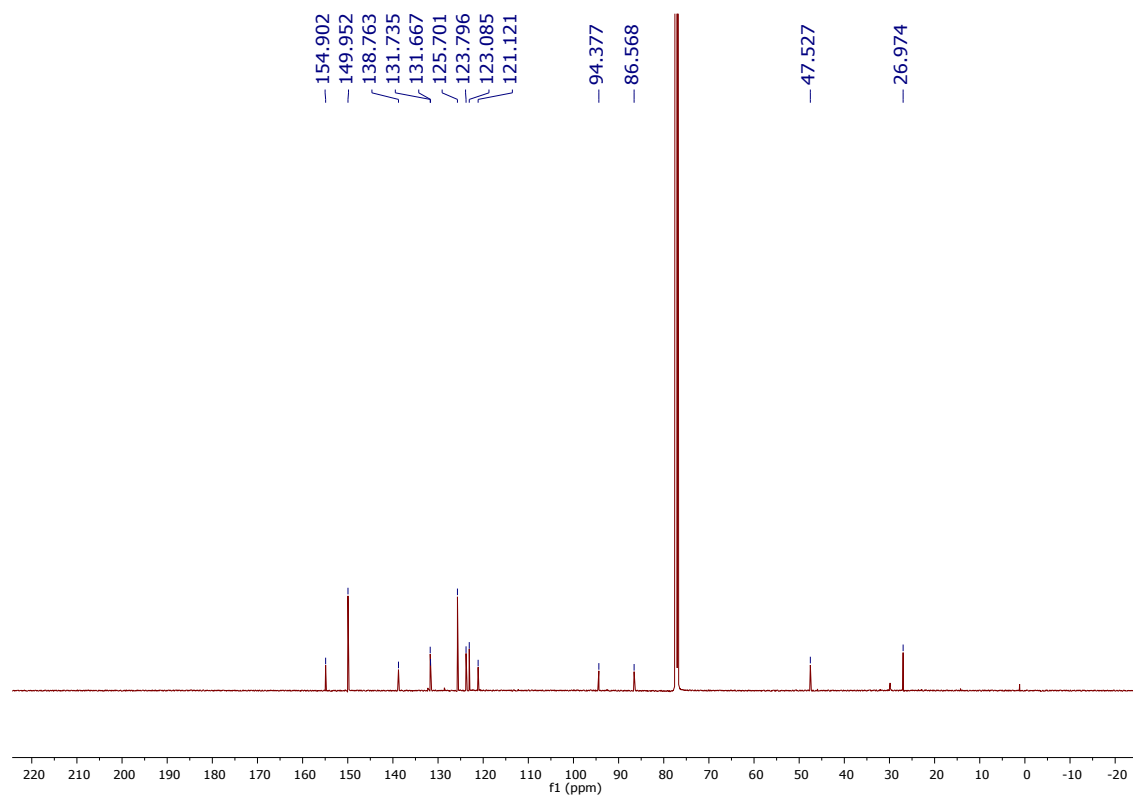


Figure S3.16. ^{13}C -NMR spectrum of *m*- $\text{CMe}_2\text{-N}$ (125 MHz, CDCl_3)

Section 4. Break Junction Experiments

4.1. Sample preparation for single-molecule experiments. Each compound was deposited onto a freshly flame-annealed gold substrate from a 0.1–1.0 mM dichloromethane solution, using an immersion time of 15 minutes for thiols and 5 minutes for pyridyls. After this time the substrate was removed and blown dry. To prepare the tip we mechanically cut a gold wire, rinse it with ethanol to remove any grease and then pass it briefly through a butane flame.

4.2. Single-Molecule Conductivity Studies. The conductance of each compound was measured using the STM-BJ method. All experiments were performed using a home-built STM, optimized for room temperature measurements in air. During the break-junction experiment, the tip is moved vertically in and out of contact with the substrate at a constant speed of approximately 10 nm/s, in 1 pm steps (we record the current at each step). For the conductance ($G = I/V$) versus distance measurements, a bias voltage V of 0.2 V was applied between the tip and the substrate. A linear current-to-voltage converter with two amplification stages allows us to record conductance values over a large dynamic range which depends on the compound under investigation and chosen to explore the largest range of conductance according to the value of the histogram peak. The gain of the first channel was 5×10^8 , and that of the second channel was 48 times larger at 2.35×10^{10} . We also placed a 12 M Ω series resistor in the main circuit to limit the total current when the junction resistance is low.

The motion of the tip and the conductance measurement are controlled by an in-house computer program to record conductance versus tip-displacement (G vs. z) curves. Typically, when moving out of contact, we move several nm after reaching our lower conductance limit. When in contact, the piezo moves a further 1–2 nm after reaching $1.0 G_0$. These limits guarantee that a broad gold contact is formed and broken in each cycle, and that any molecular junction is broken at the end of the cycle. We aim to carry out 5000–10000 approach and retraction cycles in each run, and we vary the location of the tip over the sample in order to avoid systematic errors in the data. We focus on the opening stages of the cycle. After data acquisition is complete, we first remove any blocks of traces in which there is a clear degradation in trace quality due to tip blunting or excessive build-up of material between the electrodes. We then use an automated routine to separate traces displaying plateaus from those with tunneling-only. The algorithm searches for regions of individual traces in which the amount of conductance variation is lower than a predetermined value across a certain distance interval (in practice: a plateau is identified when a $\Delta z > 0.1$ nm displays a change in conductance of $\Delta \log(G/G_0) < 0.1$ at any region below $0.5 G_0$). We use very similar criteria for all compounds.

4.3 I-V measurements. For the I-V measurements, we stop the piezo movement at defined points during the stretching of a single junction and perform a voltage ramp. This is done at set intervals (usually every 0.5 to 1 Å) during an opening trace (the precise number of I-V curves recorded depends on the length of the plateau). We aim to record several hundred molecular junctions, which generates about 10000 I-V curves, which is at the limit of what we can currently conveniently process. Between each two ramps (+V to -V and -V to +V), we return the voltage to the predetermined value and continue recording the current as the piezo is moved, thus allowing us to build a $G(z)$ trace as for the fixed-bias measurement.

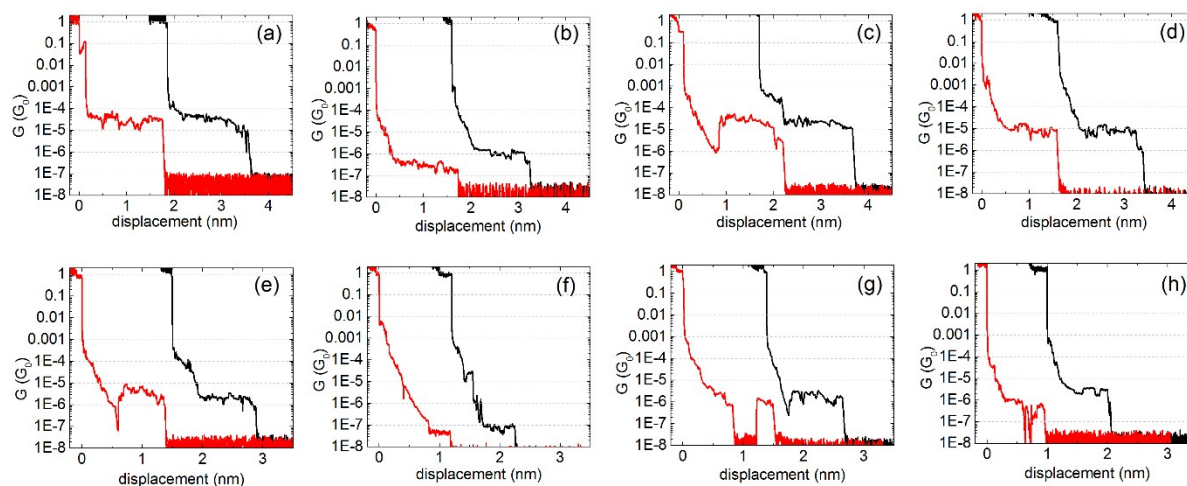


Figure S4.1. Examples of individual G vs. z traces for each compound. (a) p -CMe₂-S (b) m -CMe₂-S (c) p -CO-S (d) m -CO-S (e) p -CMe₂-N (f) m -CMe₂-N (g) p -CO-N (h) m -CO-N. In each figure, the black trace is offset laterally by 1–2 nm for clarity making the x-axis scale relative.

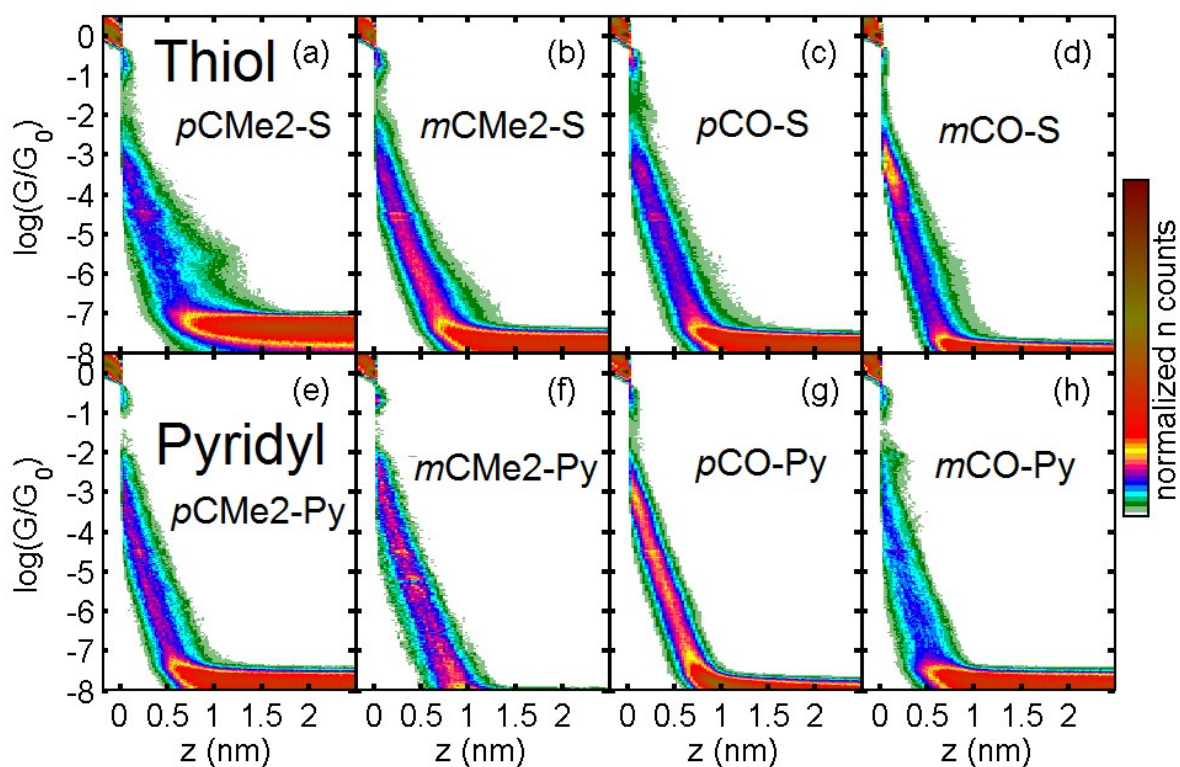


Figure S4.2. 2D histograms for the corresponding ‘no-plateau’ traces from Figure S4.1 which show only tunneling due to the lack of a molecular junction.

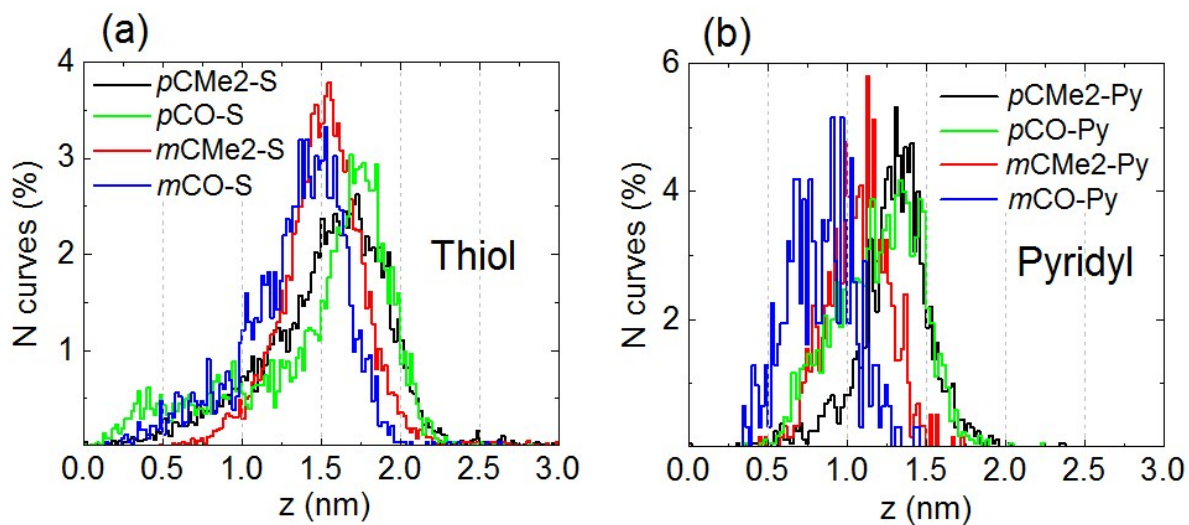


Figure S4.3. Junction length distribution histograms for (a) thiols and (b) pyridyls. The z -values are uncalibrated (without the JOC added). The distances between two Au atoms attached to the terminal S/N atoms are: *p*-CMe₂-S - 2.5 nm, *m*-CMe₂-S - 2.2 nm, *p*-CO-S - 2.5 nm, *m*-CO-S - 2.2 nm, *p*-CMe₂-N - 2.4 nm, *m*-CMe₂-N - 1.8 nm, *p*-CO-N - 2.4 nm, *m*-CO-N - 1.8 nm.

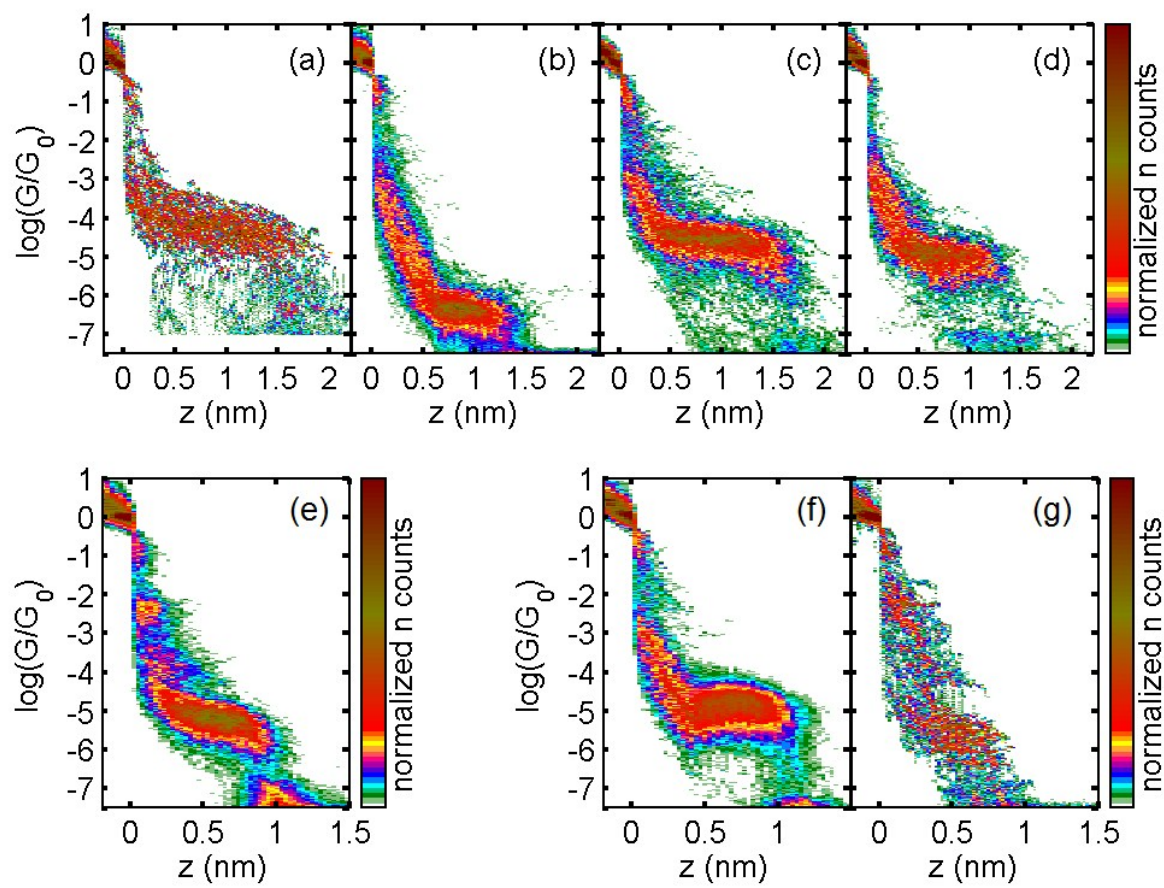


Figure S4.4. 2D histograms of the molecular junctions considered in the IV measurement. The number in each case is (a) $p\text{-CMe}_2\text{-S}$, 46; (b) $m\text{-CMe}_2\text{-S}$, 377; (c) $p\text{-CO-S}$, 275; (d) $m\text{-CO-S}$, 210; (e) $p\text{-CMe}_2\text{-N}$, 493; (f) $p\text{-CO-N}$, 267; (g) $m\text{-CO-N}$, 59.

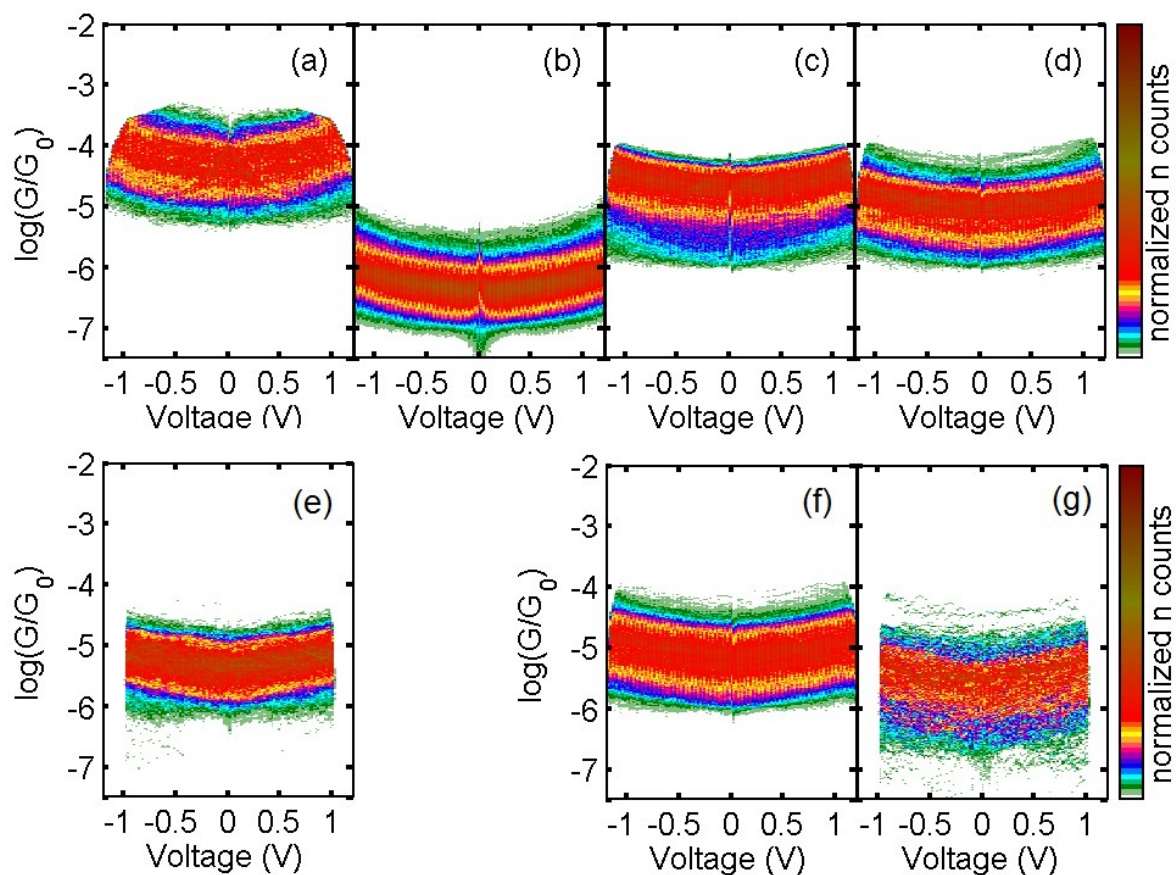


Figure S4.5. 2D histograms of the $\log(G/G_0)$ - V traces for each compound. The number of IV traces in each is (a) *p*-CMe₂-S, 3073; (b) *m*-CMe₂-S, 12984; (c) *p*-CO-S, 7967; (d) *m*-CO-S, 8005; (e) *p*-CMe₂-N, 1820; (f) *p*-CO-N, 11802; (g) *m*-CO-N, 523.

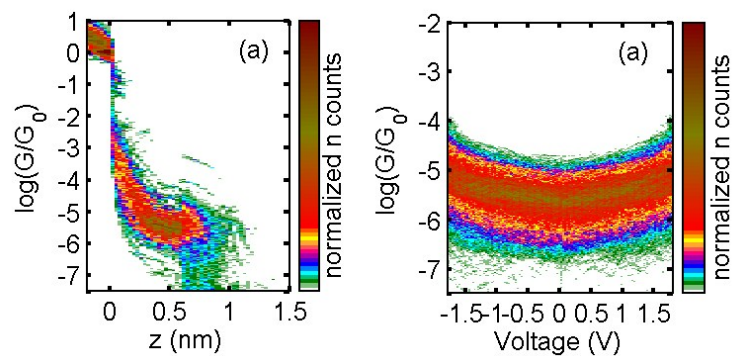


Figure S4.6. Measurement of *p*-CO-N in which we were able to ramp the bias voltage between ± 1.8 V without immediate detriment to the molecular junction.

Section 5. Computational Methods

The optimized geometry and ground state Hamiltonian and overlap matrix elements of each structure were self-consistently obtained using the SIESTA¹⁴ implementation of density functional theory (DFT). SIESTA employs norm-conserving pseudo-potentials to account for the core electrons and linear combinations of atomic orbitals to construct the valence states. The generalized gradient approximation (GGA) of the exchange and correlation functional is used with the Perdew-Burke-Ernzerhof parameterization (PBE)¹⁵, a double- ζ polarized (DZP) basis set, a real-space grid defined with an equivalent energy cut-off of 250 Ry. The geometry optimization for each structure is performed to the forces smaller than 10 meV/Å. Figures S5-1, S5-2 and S5-5 show geometry-optimized structures used to obtain the DFT results in Figure 3 and S5-3, S5-4 and S5-6. The mean-field Hamiltonian obtained from the converged DFT calculation or a simple tight-binding Hamiltonian was combined with our Gollum quantum transport code¹⁶ to calculate the phase-coherent, elastic scattering properties of the each system consist of left (source) and right (drain) leads and the scattering region. The transmission coefficient $T(E)$ for electrons of energy E (passing from the source to the drain) is calculated via the relation $T(E) = \text{Trace}(\Gamma_R(E)G^R(E)\Gamma_L(E)G^{R\dagger}(E))$. In this expression, $\Gamma_{L,R}(E) = i(\Sigma_{L,R}(E) - \Sigma_{L,R}^\dagger(E))$ describe the level broadening due to the coupling between left (L) and right (R) electrodes and the central scattering region, $\Sigma_{L,R}(E)$ are the retarded self-energies associated with this coupling and $G^R = (ES - H - \Sigma_L - \Sigma_R)^{-1}$ is the retarded Green's function, where H is the Hamiltonian and S is overlap matrix. Using obtained transmission coefficient ($T(E)$), the conductance could be calculated by Landauer formula ($G = G_0 \int dE T(E)(-\partial f/\partial E)$) where $G_0 = 2e^2/h$ is the conductance quantum, $f(E) = (1 + \exp[\frac{E - E_F}{k_B T}])^{-1}$ is the Fermi-Dirac distribution function, T is the temperature and $k_B = 8.6 \times 10^{-5}$ eV/K is Boltzmann's constant.

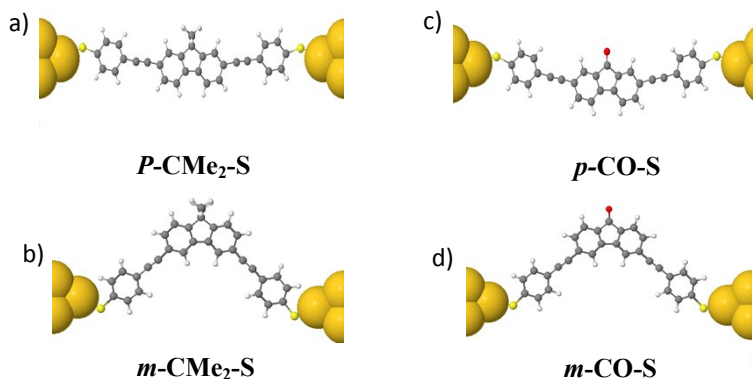


Figure S5.1. Relaxed structure of : (a,b) fluorene core connected to thiol anchor using *para* and *meta* connectivity, (c,d) fluorenone core connected to thiol anchor using *para* and *meta* connectivity.

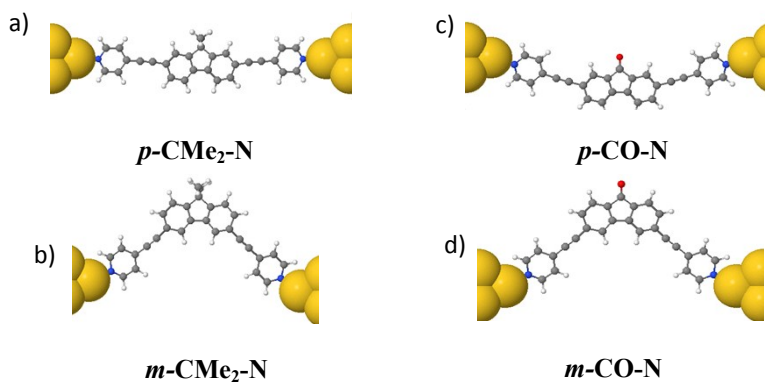


Figure S5.2. Relaxed structure of: (a,b) fluorene core connected to pyridine anchor using *para* and *meta* connectivity, (c,d) fluorenone core connected to pyridine anchor using *para* and *meta* connectivity.

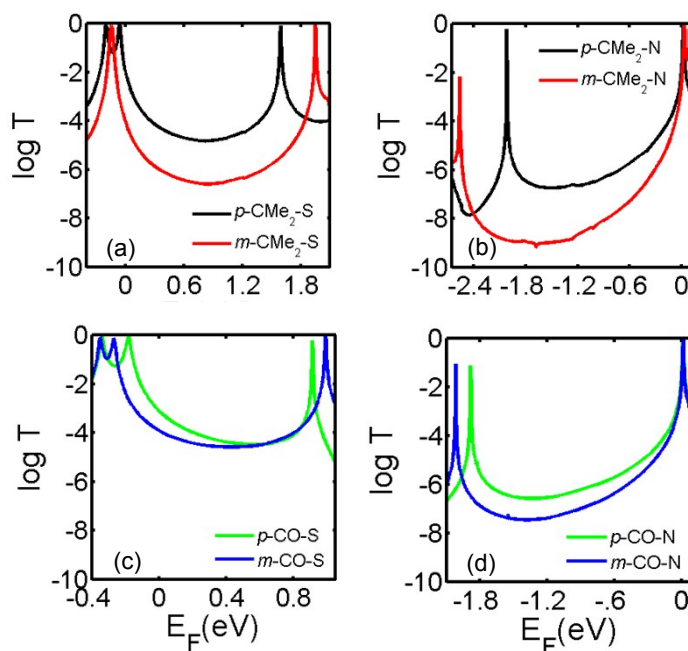


Figure S5.3. DFT transmission coefficients of (a) $p\text{-CMe}_2\text{-S}$ and $m\text{-CMe}_2\text{-S}$; (b) $p\text{-CMe}_2\text{-N}$ and $m\text{-CMe}_2\text{-N}$; (c) $p\text{-CO-S}$ and $m\text{-CO-S}$; (d) $p\text{-CO-N}$ and $m\text{-CO-N}$; connected to gold electrodes.

Figure S5.3 shows the transmission coefficients of the fluorene and fluorenone connected to gold electrodes using two different anchors. To further investigate the effect of the bridge we have also examined the conductance ratio of biphenylene with *para* and *meta* connectivities. Figures S5.4.a and b show the conductance of biphenyl with thiol and pyridine anchors. As it is clear in Figure S5.4, there is no conjugation path between two biphenyls and therefore the destructive interference with *meta* connectivity is more pronounced and as we predicted, the value of transmission coefficient of the *para* connectivity is very similar to the fluorene and fluorenone cores, which confirming our prediction that changing the bridge between two phenyl rings has no effect on *para* connectivity. Figure S5.6 shows the conductance of *para* and *meta* for all molecules.

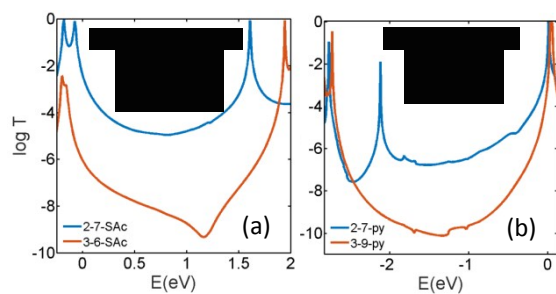


Figure S5.4. (a) Transmission coefficient of *para* connectivities (blue) and (red) for *meta* connectivities of biphenyl with thiol anchor. (b) conductance of *para* connectivities (blue) and (red) for *meta* connectivities of biphenyl with pyridine anchor.

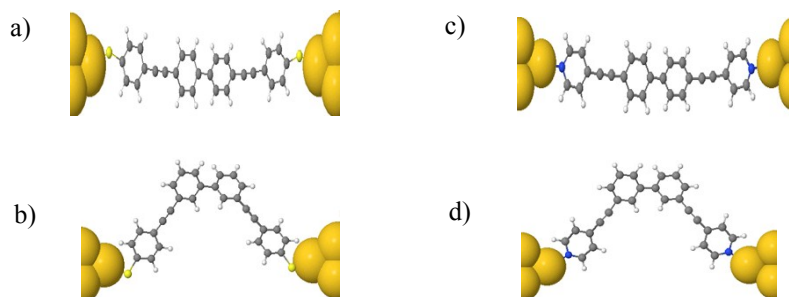


Figure S5.5. Relaxed structure of: (a, b) biphenyl core connected to thiol anchor using *para* and *meta* connectivity, (c, d) biphenyl core connected to pyridine anchor using *para* and *meta* connectivity.

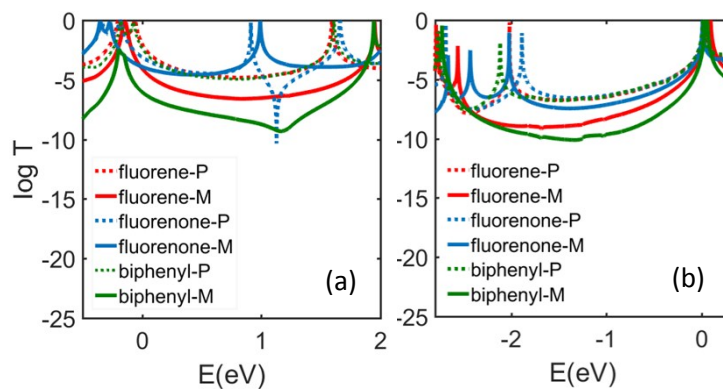


Figure S5.6. (a) conductance of *para* connectivities (dashed-line) and (solid-line) for *meta* connectivities for fluorene, fluorenone and biphenyl with thiol anchor. (b) conductance of *para* connectivities (dashed-line) and (solid-line) for *meta* connectivities for fluorene, fluorenone and biphenyl with pyridine anchor.

Section 6. Tight binding models

To demonstrate the role of the bridge in the core of the molecule, we consider the following series of tight binding models (Figure S6.1), where only nearest neighbor couplings between π -orbitals are included. The energy scale and energy origin are fixed by choosing the nearest neighbor couplings to be unity and all site energies to be zero except for the energy ϵ_9 of site number 9. For modeling a biphenyl bridge, site 9 is absent. For modeling the fluorenone, ϵ_9 is equal to 1.7 and for the fluorene ϵ_9 is equal to 5. The qualitative agreement between the material-specific results of Figure 3 and the tight-binding results of Figure 4 demonstrates that the main effect of the bridge atom is to alleviate the DQI transmission dip from the middle of HOMO and LUMO of the meta-connected biphenylene core and increase the conductance of the resulting meta-connected fluorene and fluorenone cores.

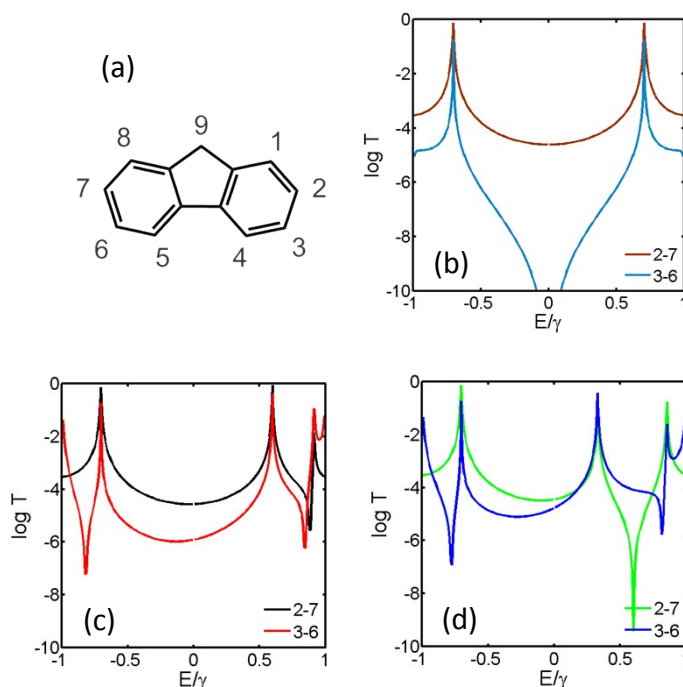


Figure S6.1. (a) Numbering system and structure considered in the TB model. (b) The transmission coefficients for biphenyl in *para* (2-7) and *meta* (3-6), (c) fluorene in *para* (2-7) and *meta* (3-6), (d) fluorenone in *para* (2-7) and *meta* (3-6) position. The value of ϵ_9 are 5 and 1.7 in b and c respectively.

Section 7. Frontier Orbitals

Table S1 shows the spatial distribution of the HOMO and LUMO orbitals of different molecules.

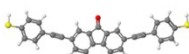
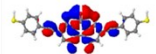
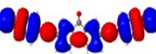
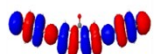
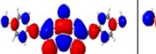
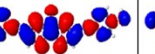
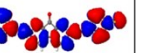

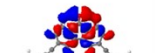




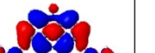
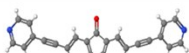
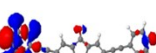
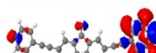

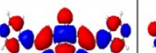
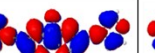
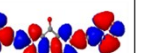
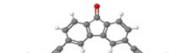
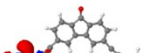
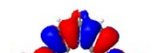
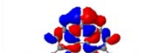

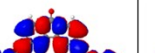


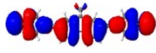
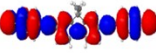
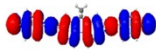
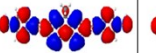
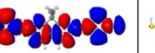
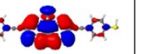
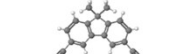




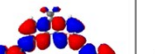

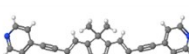
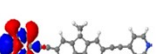

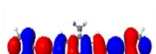

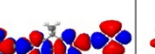
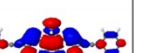
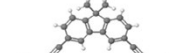
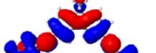

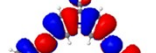
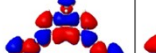
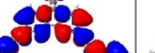
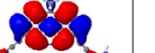
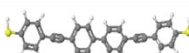


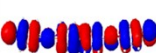
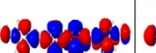
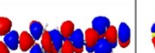
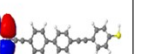
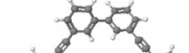

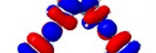
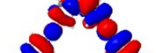
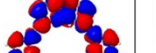
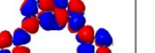
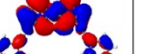
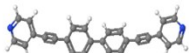
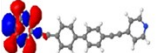
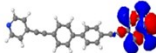

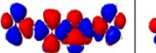
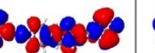
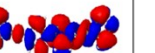
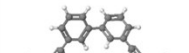
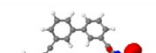
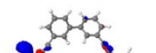
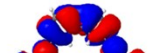
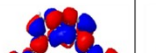
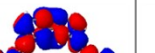
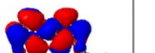
Structure	HOMO-2	HOMO-1	HOMO	LUMO	LUMO+1	LUMO+2
 2-7-9-co-SAc	 -4.91625	 -4.61268	 -4.27650	 -2.62866	 -1.96090	 -1.44897
 3-6-9-co-SAc	 -4.74448	 -4.59904	 -4.44335	 -2.62945	 -1.68954	 -1.49290
 2-7-9-co-py	 -5.23142	 -5.22989	 -5.01867	 -3.06359	 -2.45125	 -2.02582
 3-6-9-co-py	 -5.26708	 -5.15419	 -5.12535	 -3.04921	 -2.18392	 -1.89150
 2-7-9-cme2-SAc	 -5.11050	 -4.49690	 -4.11719	 -1.99006	 -1.30002	 -0.84111
 3-6-9-cme2-SAc	 -5.03681	 -4.35581	 -4.29377	 -1.65956	 -1.52583	 -1.33528
 2-7-9-cme2-py	 -5.14268	 -5.14212	 -4.73091	 -2.43463	 -1.78696	 -1.17404
 2-7-9-cme2-py	 -5.13775	 -5.13578	 -4.95868	 -2.10566	 -1.99723	 -1.65338
 Biphenyl-para-SAc	 -5.20416	 -4.49977	 -4.22742	 -1.96640	 -1.38860	 -0.77429
 Biphenyl-meta-SAc	 -5.20428	 -4.39659	 -4.37230	 -1.67703	 -1.59448	 -1.17128
 Biphenyl-para-py	 -5.16614	 -5.16584	 -4.90913	 -2.37692	 -1.86614	 -1.06742
 Biphenyl-meta-py	 -5.16912	 -5.16662	 -5.13197	 -2.13335	 -2.07916	 -1.50746

Table S1: Structure of the molecules and the corresponding frontier HOMO-LUMO orbitals calculated by DFT.

Section 8. Energy difference between the Fermi level and the molecular orbitals

The key issue here is the location of the nearest frontier orbital relative to the Fermi energy, which are sensitive to small transfers of charge between the molecule and the electrodes. Past comparisons between theory and experiment suggest that although DFT tends to predict whether or not the Fermi energy is closest to the HOMO or LUMO, the precise value is usually not known. This is due partly to unknown quantities such as the shape of the electrodes and partly due to approximations inherent in DFT. Therefore we prefer to compute quantities such as electrical conductance as functions of E_F and check whether there is a range of E_F which is consistent with experiment. In figure 3, the overall trends are consistent with a wide range of E_F and therefore our conclusions about qualitative trends are robust and do not depend on the precise value of E_F .

This uncertainty in the location of frontier orbitals relative to the Fermi energy has long been recognised by the molecular electronics community.

For example, in reference 17, the location of the nearest frontier orbital (denoted E_θ in fig 2 and eq 2 of their paper) to the Fermi energy ($E - E_F = 0$) is measured for three different molecules and for each molecule, it was found to vary widely from one experiment to another. Some of these values are shown to be in qualitative agreement with DFT calculations, provided certain electrode binding geometries are assumed. Their DFT also reveals that the precise values of E_θ depends on the spacing between the electrodes and varies along a pulling curve.

Another example from the literature, where such uncertainties are recognised is reference 18, where they state: ‘Since DFT in the generalized gradient approximation generally underestimates the HOMO-LUMO gaps of conjugated organic molecules, transmission resonances are located too close to the metal Fermi energy and molecular junctions are usually too “metallic.” However also the experimentally measured conductances are subject to uncertainties’. This paper then proceeds to make adjustments to their DFT results to obtain better agreement with experiment.

A third example is contained reference 19, where they go beyond DFT and use GW theory to study the transmission curves of naphthalene and azulene. The results do not agree with their experiments, because they cannot reliably determine E_F . They then treat E_F as a free parameter and obtain qualitative agreement with experiment by imposing a -1.5 eV shift in E_F .

The reason why the third example discusses shifting E_F , whereas the first example discusses shifting E_θ is because only the difference ($E_\theta - E_F$) matters.

Section 8. References

- (1) Shi, Z.-F.; Wang, L.-J.; Wang, H.; Cao, X.-P.; Zhang, H.-L. *Org. Lett.* **2007**, *9*, 595–598.
- (2) Gryko, D. T.; Clausen, C.; Roth, K. M.; Dontha, N.; Bocian, D. F.; Kuhr, W. G.; Lindsey, J. S. *J. Org. Chem.* **2000**, *65*, 7345–7355.
- (3) Hsung, R. P.; Babcock, J. R.; Chidsey, C. E. D.; Sib, L. R. *Tetrahedron Lett.* **1995**, *36*, 4525–4528.
- (4) Thierry, S.; Tondelier, D.; Geffroy, B.; Jacques, E.; Robin, M.; Métivier, R.; Jeannin, O.; Rault-Berthelot, J.; Poriol, C. *Org. Lett.* **2015**, *17*, 4682–4685.
- (5) Estrada, L. A.; Neckers, D. C. *J. Org. Chem.* **2009**, *74*, 8484–8487.
- (6) Price, D. W. Jr.; Tour, J. M. *Tetrahedron* **2003**, *59*, 3131–3156.
- (7) Bonakdarzadeh, P.; Topić, F.; Kalenius, E.; Bhowmik, S.; Sato, S.; Groessl, M.; Knochenmuss, R.; Rissanen, K. *Inorg. Chem.* **2015**, *54*, 6055–6061.
- (8) Song, Y.; Xu, W.; Zhu, D. *Tetrahedron Lett.* **2010**, *51*, 4894–4897.
- (9) Kobin, B.; Grubert, L.; Blumstengel, S.; Henneberger, F.; Hecht, S. *J. Mater. Chem.* **2012**, *22*, 4383–4390.
- (10) Dilmaghani, K. A.; Marjani, A. P.; Pur, F. N. *Asian J. Chem.* **2009**, *21*, 1258–1264.
- (11) Seneclauze, J. B.; Retailleaub, P.; Ziessel, R. *New J. Chem.* **2007**, *31*, 1412–1416.

- (12) Gantenbein, M.; Wang, L.; Al-jobory, A. A.; Ismael, A. K.; Lambert, C. J.; Hong, W.; Bryce, M. R. *Scientific Reports* **2017**, 7, 1794.
- (13) Quintiliani, M.; Bassetti, M.; Pasquini, C.; Battocchio, C.; Rossi, M.; Mura, F.; Matassa, R.; Fontana, L.; Russo, M. V.; Fratoddi, I. *J. Mater. Chem. C* **2014**, 2, 2517–2527.
- (14) Soler, J. M.; Artacho, E.; Gale, J. D.; García, A.; Junquera, J.; Ordejón, P.; Sánchez-Portal, D. *Journal of Physics: Condensed Matter* 2002, 14, 2745.
- (15) Perdew, J. P.; Burke, K.; Ernzerhof, M. *Physical review letters* 1996, 77, 3865.
- (16) Ferrer, J.; Lambert, C. J.; García-Suárez, V. M.; Manrique, D. Z.; Visontai, D.; Oroszlany, L.; Rodríguez-Ferradás, R.; Grace, I.; Bailey, S.; Gillemot, K. *New Journal of Physics* 2014, 16, 093029.
- (17) Zotti, L. A.; Kirchner, T.; Cuevas, J. C.; Pauly, F.; Huhn, T.; Scheer, E.; Erbe, A. *Small* **2010**, 6, 14, 1529–1535.
- (18) Bürkle, M.; Viljas, J. K.; Vonlanthen, D.; Mishchenko, A.; Schön, G.; Mayor, M.; Wandlowski, T.; and Pauly F. *Phys. Rev. B* **2012** 85, 075417.
- (19) Xia, J.; Capozzi, B.; Wei, S.; Strange, M.; Batra, A.; Moreno, J. R.; Amir, R. J.; Amir, E.; Solomon, G. C.; Venkataraman, L.; Campos, L. M. *Nano Lett.* **2014**, 14, 2941.